Influence of annealing atmosphere on photoelectrochemical response of TiO_2 nanotubes anodized under controlled hydrodynamic conditions

E. Blasco-Tamarit[a], B. Solsona[b], R. Sánchez-Tovar[b], D. García-García[a], R.M. Fernández-Domene[b], J. García-Antón[a]

[a]*Ingeniería Electroquímica y Corrosión (IEC), Instituto Universitario de Seguridad Industrial, Radiofísica y Medioambiental (ISIRYM), Universitat Politècnica de València, Camino de Vera s/n, 46022 Valencia, Spain.*

[b]*Departmento de Ingeniería Química, Universitat de València, Av de les Universitats, s/n, 46100 Burjassot, Spain*

jgarciaa@iqn.upv.es (J. García-Antón), rita.sanchez@uv.es (R. Sánchez-Tovar)

Abstract

The influence of three annealing atmospheres (air, nitrogen and argon) and the use of controlled hydrodynamic conditions (from 0 to 5000 rpm) on morphological, structural, chemical and photoelectrochemical properties of TiO_2 nanotubes have been evaluated. For this purpose, different characterization techniques have been used: Field Emission Scanning Electron Microscopy, Raman Confocal Laser Spectroscopy, Grazing Incidence X-Ray Diffraction Spectroscopy, X-Ray Photoelectron Spectroscopy, Incident Photon-to-electron Conversion Efficiency measurements, ultraviolet-visible absorption spectra, Mott-Schottky analysis and photoelectrochemical water splitting tests. According to the results, it can be concluded that both hydrodynamic conditions and annealing in non-oxidizing atmospheres improve the photoelectrochemical response of the TiO_2 nanotubes. This fact has been attributed to the oxygen vacancies formed after annealing in argon and nitrogen atmospheres and also to the presence of nitrogen into the TiO_2 lattice due to the thermal treatment in the nitrogen atmosphere.

Keywords: annealing atmosphere; anodization; hydrodynamic conditions; photoelectrochemical water splitting, TiO_2 nanotubes.

1. Introduction

Nowadays, there is a massive use of natural resources as energy sources. This fact is mainly due to the population growth and the energy dependence, especially in developed countries, and it causes serious problems. The majority of the energy produced in the world is based on fossil fuels as oil, coal and natural gas, all of them exhaustible natural resources which are responsible for environmental impacts such as climate change and resource limitations [1-3]. Therefore, there is a need in the modern world to produce a clean and economical fuel. This is the reason why most of the current research is devoted to the study of renewable energies as alternative sources of energy [3,4].

Hydrogen is the only alternative energy vector to fossil fuels that is found in abundance (not in its elemental state) in nature. Moreover, it is a non-toxic gas and it contains a higher specific energy (120 KJ g^{-1}) compared to conventional fuels, such as natural gas (50 KJ g^{-1}), or coal (29 KJ $\cdot$ g^{-1}). In addition, it is a clean energy since its combustion produces water [3,5,6]. Hydrogen cannot be found in its elemental form in nature but it can be produced by different methods, such as reforming of hydrocarbons and methanol, electrolysis of water, thermal processes or photoelectrochemical processes, among others. This study is focused on the photoelectrochemical water splitting using sunlight for hydrogen production. In this process, TiO_2 nanotubes will be used as photoanode of the process.

TiO_2 is widely used as an advanced material for applications such as solar cells, sensors, biomedicine and photocatalytic reactions [7-15]. Its good properties such as non-toxicity, chemical stability, low cost, resistance to corrosion and photocorrosion and

environmental compatibility [7, 16-22] make TiO_2 useful for these applications. In addition, TiO_2 has a band-gap position appropriate for water splitting [23]. There are several morphologies of TiO_2 nanostructures reported in the literature, such as nanoparticles, nanotubes, nanosponges, nanowires and nanorods [23]. Nanotubes were chosen for this study since this type of nanostructure presents a higher specific surface area compared to others [24] and it also presents less electron-hole pairs recombination, due to the unidirectional path to the flow of electrons. These characteristics make nanotubes suitable for several applications where nano-sizing is crucial for instance: photoelectrochemical applications such as water splitting for hydrogen production or organic pollutants removal (where nanotubes favour electron-hole separation and make a pathway to conduct electrons to the cathode) [25, 26], photoanodes in dye sensitized solar cells (to improve dye loading ability) [27] and Li-ion battery anodes (increasing the energy storage capacity of the battery) [28]. There are different methods to synthesize TiO_2 nanotubes as sol-gel methods [29, 30], hydrothermal [31], magnetron sputtering [32] or anodization [29, 33], among others. Anodization is an effective, low-cost and easy method to synthesize TiO_2 nanostructures with a high control of the physical and electrochemical properties [7, 17, 21, 23, 34-41].

The main drawback of TiO_2 is its somewhat high band gap value (~3.2 eV for anatase and ~3.0 eV for rutile), which limits its light absorption in the UV region of the solar spectrum (wavelengths smaller than 380 nm) [42, 43], which represents roughly the 5% of the solar radiation [44]. Several efforts have been made to approach the absorption of TiO_2 to the visible region to improve its photocatalytic activity, such as doping or synthesizing hybrid nanostructures [37-39, 41].

It must be taken into consideration that amorphous TiO_2 does not present photocatalytic activity. Therefore, an annealing step is necessary to transform the amorphous nanostructure into a crystalline one. This heat treatment can be carried out at different temperatures depending on the desired crystalline phase. It is well known that anatase is formed at 400 ºC and rutile appears from 500 ºC on, obtaining 100% rutile TiO_2 phase at 700ºC [45-48]. In this work, amorphous TiO_2 nanotubes will be transformed into anatase phase due to its high efficiency as a photocatalyst [35-41]. Besides, the heat treatment can be carried out using different atmospheres such as air, argon, nitrogen, oxygen or NH_3 [46, 49-54]. Thus, some works have reported the synthesis of doped TiO_2 with nitrogen using various strategies, such as the use of urea or ammonia during the sol-gel preparation [55, 56]. A different approach consists of annealing the nanostructures in a nitrogen containing atmosphere. The use of a pure nitrogen atmosphere during the heat treatment has not been widely employed as a doping method [51]. Instead, a NH_3 atmosphere is often used [57-59]. The use of N_2 instead of NH_3 to dope TiO_2 nanostructures with nitrogen presents an environmental benefit to the process. In the present study three atmospheres will be used during annealing: air, argon or nitrogen, with the novelty of combining this study with the synthesis of TiO_2 nanotubes by electrochemical anodization using controlled hydrodynamic conditions.

In this work, TiO_2 nanotubes obtained using hydrodynamic conditions during anodization annealed in different atmospheres will be studied. From our knowledge, this is the first time that the effect of rotation speed of the electrode during anodization together with the influence of annealing atmosphere have been studied for TiO_2 nanotubes. Additionally, studies found in the literature of TiO_2 nanostructures annealed in different atmospheres

that evaluate the photocatalytic performance of the nanostructures for photoelectrochemical water splitting are scarce.

Hence, the aim of this work is to study the photoeletrochemical properties of TiO_2 nanotubes synthesized by means of anodization using hydrodynamic conditions and annealed in different atmospheres: air, nitrogen and argon. In particular, the influence of both hydrodynamic conditions and annealing atmosphere have been evaluated for photoelectrochemical water splitting. The morphological and structural characterization of TiO_2 nanostructures have been carried out by Field Emission Scanning Electron Microscope, Raman Confocal Laser Spectroscopy, Grazing Incidence X-Ray Diffraction Spectroscopy (GIXRD) and X-Ray Photoelectron Spectroscopy (XPS). Incident Photon-to-electron Conversion Efficiency (IPCE) and diffuse reflectance measurements have been also performed to obtain information about the photoelectrochemical response of the nanotubes. From these techniques band gap values have been calculated. Mott-Schottky analysis, Photoelectrochemical water splitting tests and stability measurements to photocorrosion have been also carried out for the photoelectrochemical evaluation of the photocatalysts.

2. Experimental procedure

2.1. Preparation of the photocatalysts

First, 8 mm in diameter titanium rods were wet abraded with 220, 500 and 4000 silicon carbide papers. After this, each titanium sample was sonicated in ethanol for 2 minutes, cleaned with water and dried in air. Once the sample surface was clean, the Ti rod was

covered with Teflon in order to expose a surface area to the electrolyte during anodization of 0.5 cm^2.

Anodization of titanium was carried out at room temperature. For anodization, the titanium sample was the anode and a platinum foil was used as the cathode of the process. The anodization electrolyte was an ethylene glycol based solution with 0.05 M of NH_4F and 1M of H_2O. The titanium sample was connected to a Rotating Disk Electrode (RDE) to control the hydrodynamic conditions during anodization. Different rotation speeds were applied: 0 (stagnant), 2500 and 5000 rpm. A multimeter in series was also connected to register the anodization current density during the process. A potential of 55 V was applied for 30 minutes. After anodization, the titanium sample was rinsed with distilled water and ethanol and then dried with air. Finally, samples were cut in a slice of approximately 0.5 cm.

In order to transform the amorphous TiO_2 anodized nanostructures, a heat treatment was carried out. In this way, samples were annealed at 450 ºC for 1 hour to obtain anatase crystalline TiO_2 nanostructures. Different atmospheres were used (air, argon and nitrogen) to evaluate the influence of the atmosphere during the heat treatment. For annealing in argon and nitrogen atmospheres, samples were introduced in a tubular oven and the gas was bubbled for 30 minutes prior the heat treatment, in order to remove the air contained in the tube.

2.2. Morphological, structural and chemical characterization of the photocatalysts

2.2.1. Field- Emission Scanning Electron Microscopy

Field- Emission Scanning Electron Microscopy (FE-SEM) was used for the morphological characterization of the nanostructures. The microscope was an ULTRA 55 (ZEISS).

2.2.2. Raman Confocal Laser Spectroscopy

Raman Spectroscopy measurements were carried out with a Confocal Laser microscope with Raman spectroscopy (WITec). In order to determine the crystalline structure of the samples they were illuminated with a 633 nm (red laser) using 420 μW.

2.2.3. X-Ray Diffraction

X-Ray Diffraction spectra (XRD) were obtained with a Bruker D8AVANCE diffractometer with a monochromatic Cu Kα1 source.

2.2.4. *X-Ray Photoelectron Spectroscopy*

X-Ray Photoelectron Spectroscopy spectra were collected using Al-K monochromatized radiation (1486.6 eV) at 3 mA x 12 kV. The scanning step energies were 200 eV to measure the whole energy band and 50 eV to selectively measure elements.

2.3. Photoelectrochemical characterization of the photocatalysts

2.3.1. Mott-Schottky analysis

Mott-Schottky plots under dark conditions (in the absence of illumination) for the samples anodized under hydrodynamic conditions (at 5000 rpm) and annealed in air, argon and nitrogen atmospheres were obtained applying an initial potential of 0.5 $V_{Ag/AgCl}$ and

sweeping the potential from that value to -0.4 $V_{Ag/AgCl}$ at a frequency of 5 kHz. The amplitude of the signal was 10 mV.

2.3.2. Water splitting and stability measurements

Water splitting measurements were performed to evaluate which of the TiO_2 nanostructures (obtained under different hydrodynamic conditions and annealing atmospheres) presented the best photocurrent response. For this purpose, TiO_2 nanostructures were used as photoanodes in the photoelectrochemical water splitting with sunlight. Photoelectrochemical water splitting tests were carried out in a three electrode electrochemical cell connected to a potentiostat, with a 1 M KOH solution as electrolyte. The working electrode was the TiO_2 nanostructure with an exposed area of 0.26 cm^2, an Ag/AgCl (3M KCl) was the reference electrode and a platinum foil was the counter electrode. A potential scan from −0.8 $V_{Ag/AgCl}$ to 0.5 $V_{Ag/AgCl}$ with a scan rate of 2 mV s^{-1} was performed and the photocurrent density values generated were recorded by chopped light irradiation (60 s in the dark and 20 s in the light).

Stability measurements were used to evaluate the resistance of TiO_2 nanostructures to photocorrosion. In these tests, a potential of 0.5 $V_{Ag/AgCl}$ was applied under light irradiation for one hour.

2.3.3. Incident Photon-to-electron Conversion Efficiency measurements

Incident Photon-to-electron Conversion Efficiency measurements (IPCE) were used to evaluate the ratio of the number of photons incident on the nanostructures to the number of generated charge carriers. With this technique the solar spectrum range in which the

nanostructure presents the better photoelectrochemical response as photocatalyst was stablished.

The IPCE measurements were carried out using the same cell configuration as the one used in the water splitting tests in a 0.1 M Na_2SO_4 solution. During the tests, a constant potential of 0.5 $V_{Ag/AgCl}$ was applied in a wavelength range between 300 and 500 nm. The current density was registered during the IPCE measurements.

The IPCE values were calculated according to Eq. 1 [60-62]:

$$\mathrm{IPCE} = \frac{1240 \cdot \mathrm{i}}{\mathrm{P} \cdot \lambda} \cdot 100 \qquad \textbf{(1)}$$

where i is the photocurrent density ($A \cdot cm^{-2}$), P is the light power density ($W \cdot cm^{-2}$) and λ is the wavelength (nm).

The band gap of the nanostructures was calculated according to Eq. 2 (Tauc's equation) [63-65]:

$$\alpha h\nu = A\left(h\nu - E_g\right)^n \qquad \textbf{(2)}$$

where α is the absorption coefficient and for band gap measurements it is proportional to photocurrent density i ($A\ cm^{-2}$) [66, 67], $h \cdot \nu$ is the phonon energy (eV), A is a constant of the material, n is a constant depending on the electronic transition and E_g is the bang gap. For comparison, selected samples were studied by UV-VIS spectroscopy in a Cary 5000 spectrophotometer, in the 200-800 nm wavelength range, in order to estimate the band gap using the Tauc plot.

3. Results and discussion

3.1. Anodization process

The current density values vs time recorded during anodization are shown in **Figure S1**. Three different stages during the anodization process can be elucidated [68]. The current density initially decreases with time (*Stage I*) in all cases, since a compact TiO_2 layer was formed, which blocked the circulation of electrons. A minimum was reached and then the current density increased (*Stage II*) due to the formation of irregular nanopores because of the penetration of fluorides through the TiO_2 layer, which leads to the decrease of the current flow resistance. Finally (*Stage III*), the current density stabilizes due to the formation of regular nanopores or nanotubes.

Figure S1 shows that *Stage II* shortens as hydrodynamic conditions increase, indicating that the formation of nanotubes occurs faster under these conditions. That is, hydrodynamic conditions favour fluoride diffusion through the electrolyte, producing the faster arrival of these ions to the surface of titanium and favouring the nanopores formation [37]. An increase in the current density registered during anodization under hydrodynamic conditions in comparison to stagnant conditions is also observed in **Figure S1**. This increase has been attributed to the faster fluoride diffusion through the electrolyte and the subsequent increase in the oxidation reaction velocity.

3.2. Field- Emission Scanning Electron Microscopy measurements

Figure 1 shows Field- Emission Scanning Electron Microscopy (FE-SEM) images of the nanostructures obtained under different hydrodynamic conditions during anodization and annealing atmospheres (air, argon and nitrogen). The images of the nanostructures obtained under stagnant conditions (0 rpm) show an initiation layer which partially covers the top of the nanotubes. This initiation layer is related to the organic electrolyte used

during anodization [69-71] and it can cause a decrease in the absorption of solar radiation by the nanotubes, since their entrances are partially blocked. Thus, photoelectrochemical response is worsen owing to the initiation layer. **Figure 1** also shows that the initiation layer was removed as the rotation speed of the electrode during anodization increases. This behavior is observed regardless of the annealing atmosphere. Besides, the diameter of the pores of the initiation layer increased due to the flowing conditions. For instance, for nanotubes annealed in air, the average diameter of the pores increased from 50±14 nm at 0 rpm to 95±10 nm at 5000 rpm, which will result in an improvement of the photoelectrochemical response for the nanostructures anodized under hydrodynamic conditions.

Figure 2 (a) shows, as an example, images of the cross section of the TiO_2 nanotubes anodized at 5000 rpm under the different annealing atmospheres (air, argon and nitrogen). An ordered nanotubular structure can be observed owing to the control of hydrodynamic conditions by stirring the Ti electrode during anodization. The vertical arrangement of nanotubes makes possible a direct path of the incident photons and allows a higher sunlight absorption [72], which improves the TiO_2 nanotubes behavior as a photocatalyst.

Figure 2 (b) shows the nanotubes length as a function of the rotation speed (rpm) for the nanostructures obtained under the different annealing atmospheres. Note that the length of the nanotubes increases for the samples anodized under hydrodynamic conditions regardless of the annealing atmosphere. The highest lengths of the nanotubes were obtained when annealing was carried out in a nitrogen atmosphere, followed by argon atmosphere and, finally, the lowest lengths were obtained when annealing was conducted in air. It is known that as the length of the nanostructures increases, there is more surface

to absorb solar radiation [21], which improves the efficiency of the nanostructure as a photocatalyst. According to this fact, the best nanostructures for photocatalytic applications were those obtained rotating the Ti electrode during anodization at 5000 rpm and annealing the nanostructures in a nitrogen atmosphere. However, it is important to point out that with higher nanotubes length, the probability of recombination of electron-hole (e^- - h^+) pairs increases, since the path that the photon must follow until the metal surface is reached increases. Therefore, the photoelectrochemical behavior of these nanostructures should be analyzed in detail.

3.3. Raman Confocal Laser Spectroscopy measurements

Laser Confocal Microscopy with Raman spectroscopy was used to evaluate the structure of the samples.

The Raman spectra of the nanostructures was not modified by hydrodynamic conditions during anodization (see supporting information, **Figure S2**). Therefore, **Figure 3** shows, as an example, the Raman confocal laser spectra of the TiO_2 nanostructures anodized at 5000 rpm and annealed in air, nitrogen and argon. The Raman spectra of all the nanostructures present the characteristic bands of the crystalline anatase TiO_2 phase, with four peaks at around ~142, ~396, ~515 and ~640 cm^{-1} [38, 54, 55, 73-77]. These peaks confirm the transformation of amorphous TiO_2 into anatase phase after annealing.

The Raman spectra of the TiO_2 nanotubes annealed in both argon and nitrogen atmospheres present a high degree of photoluminescence. Photoluminescence was attributed to the presence of oxygen vacancies generated in the nanostructures annealed in argon and nitrogen atmospheres [41, 49, 78-80]. Annealing in the absence of oxygen (argon and nitrogen atmospheres) generates a great number of oxygen vacancies in the

nanostructures. These oxygen vacancies are the responsible for creating an excitation energy level near the bottom of the conduction band of the Ti_2O_3 lattice, where electrons can easily access [81]. This fact could explain the photoluminescence phenomena. Note that photoluminescence is greater in the nanostructures annealed in nitrogen atmosphere (**Figure 3**), since the presence of nitrogen in the TiO_2 matrix also is associated to fluorescence effect [55].

Additionally, **Figure 3** also shows that the characteristic peaks of the anatase phase appears slightly displaced to higher Raman Shifts in samples annealed in argon and nitrogen atmospheres, which is also related to the presence of oxygen vacancies generated during annealing [49, 56]. Besides, comparing the first peak characteristic of the anatase phase (~142 cm^{-1}) in all the Raman spectra, it could be observed that its width was broadened for nanotubes annealed in argon and nitrogen atmospheres with respect to the nanostructures annealed in air. This effect was related to an enhancement of crystallinity and to a smaller particle size [52, 54, 73]. The improvement in crystallinity is beneficial for photoelectrocatalytic applications [82].

Both the presence of photoluminescence in the Raman spectra and the widening of the main characteristic peak of the anatase phase for the nanostructures annealed in nitrogen also suggest the presence of nitrogen atoms in the matrix of the crystalline oxide [55, 82]. XPS measurements were carried out (and presented below) to clarify this.

In order to evaluate in detail the crystalline and the chemical structure of the nanostructures annealed in the different atmospheres, grazing incidence X-ray diffraction and X-ray photoelectron spectrometry measurements were carried out for the

nanostructures anodized at 5000 rpm, since no significant differences were detected for the Raman spectra of the samples anodized at the different rotation speeds.

3.4. X-Ray Diffraction measurements

Figure S3 shows the XRD patterns of the TiO_2 samples anodized at 5000 rpm and annealed in the three different atmospheres. In this figure, apart from the diffractions of metallic titanium, typical peaks of the TiO_2 anatase phase have been identified. In particular, peaks appeared at 2θ = ~25.5, ~38.2, ~48.2, ~53.1 and ~54.2 °, corresponding to the (101), (004), (200), (105) and (211) planes of the anatase phase [83]. The preferred orientation for all the samples is that related to the (101) plane and the high intensity of this peak shows enhanced crystallinity for the TiO_2 nanotubes annealed in both nitrogen and argon atmospheres. These results are in agreement with those obtained by Raman spectroscopy. This higher intensity of the TiO_2 reflections in O-free conditions can be related to the higher length of the nanotubes as observed by microscopy (**Figure 2**). Therefore, it is likely that an increase in crystallinity might be beneficial for the photoelectrocatalytic activity improvement.

Crystallite size was calculated according to Scherrer's equation [84, 85] using the main anatase X-ray diffraction peak (101) and it was ca. 23 nm regardless the annealing atmosphere used.

3.5. X-Ray Photoelectron Spectroscopy measurements

The near surface of selected synthesized samples has been studied by XPS. The XPS spectra of Ti 2p (**Figure 4)**, O 1s (**Figure 5)** and N 1s (**Figure 6)** for TiO_2 nanotubes anodized at 5000 rpm and annealed in air (a), nitrogen (b) and argon atmospheres (c) have been represented. After deconvolution and fitting operations of the Ti 2p XPS spectrum

(**Figure 4)**, four peaks were obtained at around 457.1, 458.3, 462.9 and 464.1 eV. The peaks at 458.3 eV and 464.1 eV correspond to the spin-orbital splitting photoelectrons of Ti^{4+} in Ti $2p_{1/2}$ (titanium oxide), while the peaks at 457.1eV and 462.9 eV correspond to Ti^{3+} in Ti $2p_{3/2}$ (titanium suboxide) [86, 87]. Considering the area under the curve of each of these deconvoluted peaks, the amount of Ti^{3+} and Ti^{4+} has been estimated (**Table 1)**. The amount of the non-stoichiometric titanium (Ti^{3+}) is higher in the samples annealed in nitrogen and argon atmospheres compared to that annealed in air atmosphere. This fact must be associated with the absence of oxygen during the heat treatment in those atmospheres, which produces oxygen vacancies.

Figure 5 shows the XPS spectra of O 1s for TiO_2 nanotubes anodized at 5000 rpm and annealed in air (a), nitrogen (b) and argon atmosphere (c) respectively. Three peaks were obtained after deconvolution at around 529.7, 531.4 and 532.7 eV. The peak located at 529.7 corresponds to lattice oxygen (L_O), which is associated to O^{2-} atoms fully coordinated with Ti^{4+}. The oxygen vacancies (V_O) have been obtained after the de-convolution of the O 1s narrow scan at 531.4 eV. The peak located at 532.7 corresponds to chemisorbed oxygen (C_O), which is associated to dissociating oxygen of OH from H_2O, surface oxygen species from carbonates or O_2 on TiO_2 surface [86, 88-90]. **Table 2** shows the relative amount of each O species after the deconvolution of the XPS O1s peaks. The peak associated with lattice oxygen (around 529.7 eV) is higher when the TiO_2 is annealed in an atmosphere with oxygen (air atmosphere). The highest area related to oxygen vacancies (531.4 eV) was obtained annealing in argon and, especially, in nitrogen atmospheres. The increase of oxygen vacancies is in agreement to the increment of the concentration of non-stoichiometric titanium (Ti^{3+}) observed in **Table 1**. The presence of a more intense peak corresponding to dissociating oxygen or OH species from H_2O or

-O_2 (peak around of 532.7 eV) observed when the TiO_2 nanotubes were annealed in the absence of oxygen (nitrogen and argon atmospheres), could be also related to a higher amount of surface defects, since they are associated to OH species on the surface [86, 88-90].

Figure 6 shows the spectra of N 1s for the TiO_2 nanotubes anodized at 5000 rpm and annealed in air (a), nitrogen (b) and argon atmosphere (c) respectively. First of all, it must be noted that the assignment of the XPS peaks to the different N-species is highly controversial in the literature [91-95]. However, in our work some clear trends that allow us to draw important conclusions can be observed. Peaks around 398.2 eV and 399.2 eV have been obtained after deconvolution in the samples treated in air or argon. It can be observed that the energy of these peaks is higher in the case of the sample treated in a nitrogen atmosphere, shifting to values around 399.0 eV and 400.2 eV. Several authors attribute this displacement to the change in the nitrogen electronegativity when it is present in the lattice. In this case, nitrogen becomes an electron donor instead of an electron acceptor. Therefore, nitrogen becomes positively charged. Nitrogen ions at high energy (400.2 eV) transfer electrons to adjacent oxygen atoms more easily due to their low electronegativity compared to those oxygen atoms. The positively charged nitrogen ions correspond to the following bonds: N-Ti-O and Ti-O-N-O [91-95]. This effect is observed when the sample is annealed in a nitrogen atmosphere. Overall, the amount of nitrogen in the surface detected by XPS increases by a factor of ca. 2 in the sample annealed in N_2 compared to the others. Moreover, the areas under the curves of the deconvoluted peaks of N 1s for the TiO_2 nanotubes annealed in the different atmospheres, have been calculated (**Table 3**), showing that the presence of nitrogen in the structure

clearly increases when the sample is annealed in nitrogen atmosphere, obtaining the largest area in the peak with less energy in that case.

3.6. Mott-Schottky analysis

The total capacitance of a semiconductor/electrolyte interface can be described by the Mott-Schottky equation, which for an *n*-type semiconductor such as TiO_2, is:

$$\frac{1}{C^2} = \frac{1}{C_H^2} + \frac{2}{\varepsilon\varepsilon_0 e N_D}\left(E - E_{FB} - \frac{kT}{e}\right) \quad (3)$$

where C_H is the capacitance of the Helmholtz layer, ε is the dielectric constant of TiO_2 (a value of 100 has been used for TiO_2 nanostructures [96, 97]), ε is vacuum permittivity ($8.85 \cdot 10^{-14}$ F cm^{-1}), e is electron charge ($1.60 \cdot 10^{-19}$ C), N_D is the density of donor species within the semiconductor, E_{FB} is the flat-band potential, k is the Boltzmann constant ($1.38 \cdot 10^{-23}$ J/K) and T is absolute temperature.

Figure 7 shows the Mott-Schottky plots (C^{-2} vs. E diagrams) of the three TiO_2 samples anodized at 5000 rpm and annealed in different atmospheres (air, argon and nitrogen). The three plots show a linear region with positive slope, which indicates *n*-type semiconductivity, as expected. Nevertheless, there are important differences between these curves. The linear region slope for the sample annealed in an air atmosphere is notably higher than those for the other two samples. According to Eq. 3, the slope of the C^{-2} vs. E representation is inversely proportional to the donor density, N_D. Therefore, the sample annealed in air has a lower concentration of electron donor species than the samples annealed in argon and nitrogen. Values of N_D for the three samples are the

following: $1.47 \cdot 10^{19}$ cm^{-3} for the sample annealed in air, $3.45 \cdot 10^{19}$ cm^{-3} for the sample annealed in argon and $4.98 \cdot 10^{19}$ cm^{-3} for the sample annealed in nitrogen. N_D values are in good agreement with the ones obtained for TiO_2 nanotubes in other studies [98, 99]. Oxygen vacancies have usually been reported as the major donor species in TiO_2 [97, 100-102]. The values of N_D obtained for the three samples imply, consequently, that samples annealed in argon and nitrogen atmospheres (especially the last one) have more oxygen vacancies within their structure than the sample annealed in air. This result is consistent with XPS data, thus confirming the increment in oxygen vacancies in the samples thermally treated in oxygen-free atmospheres. The implications of these conclusions will be studied in the following sections, which deal with the photoelectrochemical characterization of the samples.

3.7. Water splitting and stability measurements

The synthetized TiO_2 nanotubes have been used as photoanodes for photoelectrochemical water splitting. **Figure 8** shows the photoelectrochemical response for the nanostructures anodized at different rotation speeds (0, 2500 and 5000 rpm) and annealed under different atmospheres (air, nitrogen and argon). A peak in the photocurrent density values registered at the beginning of each pulse was observed in most of the samples mainly between -0.8 $V_{Ag/AgCl}$ and -0.4 $V_{Ag/AgCl}$. This peak is associated with the recombination process of the generated electron and holes. This peak disappears at higher applied potentials (~ - 0.2 $V_{Ag/AgCl}$) when constant photocurrent density values are reached [103]. In general, the photocurrent density values stabilize as the potential shifts towards more positive values. This fact allows to carry out the photoelectrochemical water splitting applying low polarizations. Besides, **Figure 8** shows that photocurrent densities under

dark conditions are on the order of 0 $\mu A/cm^2$, which indicates that nanostructures are stable after light application (there is no electrochemical oxidation). When the light is switched on again, the photocurrent densities increase quickly, which may be related to a rapid transport of the charges inside the photocatalyst [104].

Figure 8 also shows that for the nanotubes annealed under the different atmospheres, photocurrent densities increase as the rotation speed of the Ti electrode during anodization increased. This fact reveals that the use of hydrodynamic conditions during anodization improves the photoelectrochemical behavior of the obtained nanotubes. This might be attributed to different causes: on the one hand, FE-SEM images (**Figure 1**) showed that hydrodynamic conditions used during anodization partially removed the initiation layer formed on the top of the nanotubes, allowing a higher absorption of solar radiation which resulted in an increase in the photocurrent densities. On the other hand, **Figure 2b** shows an increase in the length of the nanotubes as the rotation speed during the anodization increases, which leads to an increase in the solar radiation absorption surface [21] and therefore an increase in the photocurrent densities.

Regarding the atmosphere used during annealing, **Figure 8** shows that the highest photocurrents were registered for nanostructures treated in argon and nitrogen. Moreover, the highest photocurrent densities are obtained for the nanostructures anodized under hydrodynamic conditions. The photocurrent values are directly related to the amount of oxygen produced in the photoanode and according to the Faraday's Law with the hydrogen generated in the cathode. Therefore, high photocurrents are associated with high hydrogen production in order to use these nanostructures in the photoelectrochemical water splitting process. The presence of a high number of oxygen

vacancies in the nanostructures annealed in nitrogen and argon atmospheres may increase the conductivity of the samples resulting in a better photoelectrochemical performance. Additionally, for a better photoelectrochemical characterization of the nanostructures annealed at the different atmospheres, IPCE and Ultraviolet-Visible absorption measurements are presented in the next sections.

The photostability of the nanostructures under a constant applied potential of 0.5 $V_{Ag/AgCl}$ under light conditions for one hour was evaluated. **Figure S4** shows stable photocurrent transients with time for all the samples, which means that the nanostructures are stable to photocorrosion. Additionally, samples were observed by FE-SEM before and after the photoelectrochemical tests and no appreciable differences were observed. **Figure S4** also shows the increase in the photocurrent densities for nanostructures anodized under hydrodynamic conditions.

According to all these facts, nanotubes anodized at 5000 rpm and annealed in nitrogen and argon atmosphere are the most suitable for being used as photoanodes in photoelectrochemical water splitting applications.

3.8. Incident Photon-to-electron Conversion Efficiency measurements

To fully characterize the photoelectrochemical properties of the synthesized nanostructures and relate them to their photocatalytic performance, incident Photon-to-electron Conversion Efficiency (IPCE) measurements have been carried out.

The IPCE measurements were calculated according to Eq.1 and they allow establishing the number of electrons generated as a result of the flow of photons that impinges on the

nanostructures, for each wavelength. **Figure 9 (a)** shows, as an example, the IPCE values of the nanotubes anodized at 5000 rpm and annealed under the different atmospheres. This figure shows that nanostructures annealed in nitrogen atmosphere achieve the highest IPCE values followed by those annealed in argon atmosphere. The lowest IPCE values were obtained annealing in air atmosphere. This behavior was also observed under stagnant conditions and for the nanotubes anodized at 2500 rpm (**Figure S5**).

Figure 9 (a) also shows that the nanotubes annealed in air atmosphere do not present photocatalytic response at wavelengths higher than 380 nm, that is, these photocatalysts can only absorb wavelengths from the UV region of the solar spectrum. However, nanotubes annealed in argon atmosphere can absorb some radiation of slightly higher wavelengths (up to 390 nm), approaching the visible region. This improvement in the absorption range of the photocatalyst annealed in argon (non-oxidizing atmospheres) may be due to the higher amount of oxygen vacancies. XPS measurements (**Table 1** and **Table 2**) confirmed that the density of the oxygen vacancies in the TiO_2 samples increased with the decrease in oxygen content during the heat treatment [54, 73], that is, they increased when heat treatment was carried out in argon compared to air atmosphere. Indeed, the increase in oxygen vacancies corresponds to a higher density of electron donors, which facilitates the process of separation and transport of charges and improves the efficiency of the electron-hole pairs [49, 51]. Therefore, a higher oxygen vacancy density in the nanostructure could contribute not only to improve the electron conductivity and to facilitate the charge transfer, but also to achieve a slight absorption of visible light [49]. In the case of the nanotubes annealed in nitrogen atmosphere, **Figure 9 (a)** shows that these nanostructures can absorb a small amount of light in the visible region of the solar spectrum, since low photocurrents are registered for wavelengths up to 400 nm. XPS

measurements (**Table 1** and **Table 2**) and Mott-Schottky analysis (**Figure 7**) demonstrated that oxygen vacancies also increased by the thermal treatment in a nitrogen atmosphere (absence of oxygen) compared to those generated in air atmosphere. Besides, for nanostructures annealed in nitrogen, both the analysis of the crystalline phase using confocal Raman microscopy (**Figure 3**) and the XPS measurements (**Table 3**), showed the presence of nitrogen atoms into the structure of TiO_2. Therefore, the increase in the photo-activity of TiO_2 annealed in nitrogen atmosphere under simulated solar radiation could be attributed to both the increase of oxygen vacancies and the presence of nitrogen in the structure of TiO_2, which may cause greater crystallization or a decrease in the band gap of the semiconductor [82].

The modification of the band gap value due to the annealing atmosphere will be discussed in detail below.

The IPCE results are in agreement with the water splitting measurements since the highest photoresponses were achieved for the nanostructures annealed in argon and nitrogen atmospheres (**Figure 8**). Other authors [105] observed that the presence of N into the TiO_2 matrix can also stress the nanostructure, resulting in lower photocurrents for samples annealed in nitrogen in comparison to the ones annealed in argon. This might be the reason why photocurrents are slightly higher for samples annealed in argon atmosphere.

Band gap energy values were also obtained from the Incident Photon-to-electron Conversion Efficiency measurements according to Eq. 2 (Tauc's equation) and following the procedure explained by the authors in a previous works [38]. In Eq.2 the value of n is considered 2 since literature indicates that anatase TiO_2 has only an indirect band gap

[106], being 2 the n value for an indirect allowed transition in this case. According to this, the indirect band gap can be calculated from the intercept of the two linear regions of the representation of $(\alpha \cdot h \cdot \nu)^{1/2}$ vs. photon energy. **Figure 9 (b)** shows, as an example, the plot for the band gap calculation for the nanostructures anodized at 5000 rpm at the different atmospheres. The band gap values of the different nanostructures have been calculated from this figure and they are shown in **Table 4**. All of them were lower than the band gap of anatase crystalline TiO_2 (~3.2 eV according to literature [37, 106, 107]), and they were similar independently of the rpm used during the anodization process. In relation to the annealing, the highest band gap values were obtained annealing with air (in fact these values are close to the ones of anatase) and the lowest ones were obtained annealing with nitrogen. This fact suggests that the presence of nitrogen in the oxide matrix may reduce the band gap of the photocatalyst, leading to a better absorption in the visible region of the solar spectrum, and therefore to an increase in the photo-activity of the nanostructures. Consequently, a decrease in the band gap is expected in photocatalysts that include nitrogen in their matrix [55,56]. These facts are in good agreement with the IPCE (**Figure 9 (a)**) and water splitting (**Figure 8**) results, respectively. It must be noted that band gaps estimated by UV-Vis. spectroscopy on the samples annealed in different atmospheres and using 5000 rpm corroborate the values obtained by IPCE, resulting in 3.10, 3.03 and 2.93 eV for samples treated in air, argon and nitrogen, respectively.

The worst photocatalytic responses (**Figure 8**) were obtained for the nanostructures annealed in air atmosphere (~ 21% oxygen and 79 % nitrogen) probably due to the fact that the amount of nitrogen present in their matrix is low (**Figure 3** and **Table 3**), and, therefore, the band gap is higher than that observed in nanostructures annealed in nitrogen atmosphere. Moreover, the amount of oxygen vacancies is the lowest in comparison to

the nanostructures annealed in both nitrogen and argon atmospheres, (**Table 1**, **Table 2** and **Figure 7**).

4. Conclusions

Current density measurements during anodization revealed that the formation of nanotubes occurred faster under hydrodynamic conditions regardless of the atmosphere used during the heat treatment (air, argon or nitrogen).

FE-SEM images showed that the initiation layer formed on the top of the nanotubes was removed as the rotation speed during anodization increases. This behaviour was observed independently of the annealing atmosphere.

The highest length of the nanotubes was obtained when annealing was carried out in a nitrogen atmosphere, while the lowest were obtained in air.

The Raman spectra of all the nanostructures were characteristic of the anatase phase of crystalline TiO_2 and it was not modified due to hydrodynamic conditions. However, differences in the concentration of oxygen vacancies were observed depending on the annealing atmosphere used. Then, TiO_2 nanotubes annealed in both argon and nitrogen atmospheres confirm the increase in the formation of oxygen vacancies compared to the nanotubes formed in air. Interestingly, the presence of nitrogen atoms in the matrix of the crystalline oxide can also be proposed in the sample annealed in nitrogen. Both XRD and Raman data suggest an enhancement of crystallinity in the nanostructures when annealing was performed in non-oxidizing atmospheres.

XPS measurements indicated a high concentration of oxygen vacancies and a higher amount of surface defects when the TiO_2 nanotubes were annealed in absence of oxygen (nitrogen and argon atmospheres). Additionally, the presence of surface nitrogen in the structure was the highest when the sample was annealed in nitrogen atmosphere. The increase in oxygen vacancies within the structure of samples annealed in argon and nitrogen atmospheres, compared with TiO_2 nanotubes annealed in air, was also corroborated by Mott-Schottky analysis, which allowed calculating the donor density, N_D.

Nanotubes annealed in air atmosphere do not present photocatalytic response at wavelengths greater than 380 nm. However, nanotubes annealed in argon atmosphere absorb some radiation up to 390 nm. This improvement in the absorption ranges of the photocatalyst was attributed to the oxygen vacancies generated by annealing in argon. Nanotubes annealed in nitrogen atmosphere absorbed a small amount of light in the visible region of the solar spectrum, since low photocurrents are registered for wavelengths up to 400 nm. This fact could be attributed to both the increase of oxygen vacancies and the incorporation of nitrogen into the structure of TiO_2, which leads to a decrease in the band gap of these nanostructures and consequently to an increase in their photo-activity.

These results confirm that the use of a nitrogen or argon atmospheres during the heat treatment increases the photocatalytic activity of the nanotubes for the photoelectrochemical water splitting. Furthermore, if these conditions are combined with nanotubes anodized under controlled hydrodynamic conditions, a greater improvement is obtained in the photocatalytic response of the nanostructures.

Acknowledgments:

The authors would like to express their gratitude for the financial support to the "Generalitat Valenciana (GV/2020/044)" as well as to the "Agencia Estatal de Investigación" (Project Code: PID2019-105844RB-I00/ AEI/10.13039/501100011033)", for its help in the Laser Raman Microscope acquisition (UPOV08-3E-012) and the co-finance by the European Social Fund. Authors from UV also thank MINECO (MAT2017-84118-C2-1-R project) and FEDER for funding.

Tables caption

Table 1. Ti^{4+} and Ti^{3+} at.% obtained from the XPS areas of the nanostructures anodized at 5000 rpm and annealed in air, nitrogen and argon atmospheres.[a]

Table 2. Relative amount of the different surface oxygen species (area %) obtained from the XPS areas of the nanostructures anodized at 5000 rpm and annealed in air, nitrogen and argon atmospheres.

Table 3. N 1s peak areas obtained from XPS measurements of the nanostructures anodized at 5000 rpm and annealed in air, nitrogen and argon atmospheres.

Table 4. Band gap values of the nanostructures obtained under different hydrodynamic conditions during anodization and annealed in air, nitrogen and argon atmospheres.

Figures caption

Figure 1. FE-SEM images of the nanostructures obtained under different hydrodynamic conditions during anodization and annealing atmospheres (air, nitrogen and argon).

Figure 2. (a) FE-SEM images of the cross section of the TiO_2 nanotubes anodized at 5000 rpm under the different heat treatments (air, nitrogen and argon). (b) Nanotubes length as a function of the rotation speed (rpm) for the nanostructures obtained under the different heat treatments (air, nitrogen and argon).

Figure 3. Raman confocal laser spectra of TiO_2 nanostructures anodized at 5000 rpm and annealed in different atmospheres (air, nitrogen and argon).

Figure 4. XPS spectra of Ti 2p for the TiO_2 nanostructures anodized at 5000 rpm and annealed in air atmosphere (a), nitrogen atmosphere (b) and argon atmosphere (c).

Figure 5. XPS spectra of O 1s for the TiO_2 nanostructures anodized at 5000 rpm and annealed in air atmosphere (a), nitrogen atmosphere (b) and argon atmosphere (c).

Figure 6. XPS spectra of N 1s for the TiO_2 nanostructures anodized at 5000 rpm and annealed in air atmosphere (a), nitrogen atmosphere (b) and argon atmosphere (c).

Figure 7. Mott-Schottky plots for the nanostructures anodized at a rotation speed of 5000 rpm and annealed in air, argon and nitrogen.

Figure 8. Water splitting measurements for the nanostructures anodized at different rotation speeds (0, 2500 and 5000 rpm) and annealed under different atmospheres (Air, Nitrogen and Argon).

Figure 9. (a) Incident photon-to-electron conversion efficiency and (b) band gap measurements obtained from IPCE tests of the nanostructures anodized at 5000 rpm and annealed under different atmospheres (Air, Nitrogen and Argon).

REFERENCES:

[1] S. Ashrafi, M. Mousavi-Kamazani, S. Zinatloo-Ajabshir, A. Asghari, Novel sonochemical synthesis of $Zn_2V_2O_7$ nanostructures for electrochemical hydrogen storage, Int. J. Hydrog. Energy 45 (2020) 21611-21624. https://doi.org/10.1016/j.ijhydene.2020.05.166

[2] A. G. Stern, A new sustainnable hydrogen clean energy paradigm, Int. J. Hydrog. Energy 45 (2018) 4244-4255. https://doi.org/10.1016/j.ijhydene.2017.12.180

[3] J.D. Fonseca, M. Camargo, J.M. Commenge, L. Falk, I.D. Gil, Trends in design of distributed energy systems using hydrogen as energy vector: A systematic literature review, Int. J. Hydrog. Energy. 4 (2019) 9486–9504. https://doi.org/10.1016/j.ijhydene.2018.09.177

[4] M. Masjedi-Arani, M. Ghiyasian-Arani, O. Amiri, M. Salavati-Niassari, CdSnO3-graphene nanocomposites: ultrasonic synthesis using glucose as capping agent and characterization for electrochemical hydrogen storage, Ultrason. Sonochem., 61 (2020) 104840-104852. https://doi.org/10.1016/j.ultsonch.2019.104840

[5] S.B. Patil, P.S.Basavarajappa, N. Ganganagappa, M.S. Jyothi, A.V. Raghu, K.R. Reddyd, Recent advances in non-metals-doped TiO_2 nanostructured photocatalysts for visible-light driven hydrogen production, CO_2 reduction and air purification, Int. J. Hydrog. Energy 44 (2019) 13022-13039. https://doi.org/10.1016/j.ijhydene.2019.03.164

[6] M. D. Cabezas, A. E. Frak, A. Sanguinetti, J. I. Franco, and H. J. Fasoli, Hydrogen energy vector: Demonstration pilot plant with minimal peripheral equipment, Int. J. Hydrog. Energy 39 (2014) 18165–18172. https://doi.org/10.1016/j.ijhydene.2014.09.040

[7] Z. Jedi-Soltanabadia, M. Ghorannevissb, Z. Ghorannevisc, H. Akbaria, Anodic

growth of Nitrogen-doped Titanium dioxide nanotubes by anodization process of elemental Titanium in ethylene glycol based electrolyte solution with different water contents, Vacuum 155 (2018) 387–390. https://doi.org/10.1016/j.vacuum.2018.06.027

[8] N. Nyein, W.K. Tan, G. Kawamura, A. Matsuda, Z. Lockman, TiO2 nanotube arrays formation in fluoride/ethylene glycol electrolyte containing LiOH or KOH as photoanode for dye-sensitized solar cell, J. Photochem. Photobiol., A 343 (2017) 33–39. https://doi.org/10.1016/j.jphotochem.2017.04.015

[9] P. Dwivedi, N. Chauhan, P.V. kanandan, S. Das, D.S. Kumar, S. Dhanekar, Scalable fabrication of prototype sensor for selective and sub-ppm level ethanol sensing based on TiO2 nanotubes decorated porous silicon, Sens. Actuators, B 249 (2017) 602–610. https://doi.org/10.1016/j.snb.2017.03.154

[10] S.B. Patel, N. Baker, I. Morques, et al., Transparent TiO2 nanotubes on zirconia for biomedical applications, RSC Adv. 7 (2017) 30397–30410. https://doi.org/10.1039/C7RA03940A

[11] J. Low, S. Qiu, D. Xu, C. Jiang, B. Cheng, Direct evidence and enhancement of surface plasmon resonance effect on Ag-loaded TiO2 nanotube arrays for photocatalytic CO2 reduction, Appl. Surf. Sci. 434 (2018) 423–432. https://doi.org/10.1016/j.apsusc.2017.10.194

[12] C. Ampelli, F. Tavella, S. Perathoner and G. Centi, Engineering of photoanodes based on ordered TiO2-nanotube arrays in solar photo-electrocatalytic (PECa) cells, Chem.Eng. J. 320 (2017) 352–362. https://doi.org/10.1016/j.cej.2017.03.066

[13] M. Wang, J. Ioccozia, L. Sun, C. Lin, Z. Lin, Inorganic-modified semiconductor TiO2 nanotube arrays for photocatalysis, Energy Environ. Sci. 7 (2014) 2182–2202. https://doi.org/10.1039/C4EE00147H

[14] D. Regonini, C.R. Bowen, A. Jaroenworaluck, R. Stevens, A review of growth mechanism, structure and crystallinity of anodized TiO2 nanotubes, Mater. Sci. Eng. R Reports. 74 (2013) 377–406. https://doi.org/10.1016/j.mser.2013.10.001

[15] E. Roduner, Size matters: Why nanomaterials are different, Chem. Soc. Rev. 35 (2006) 583–592. https://doi.org/10.1039/b502142c.

[16] X. Wang, Z. Li, J. Shi, Y. Yu, One-dimensional titanium dioxide nanomaterials: nanowires, nanorods, and nanobelts, Chem. Rev. 114 (2014) 9346–9384. https://doi.org/10.1021/cr400633s

[17] K. Indira1, U. Kamachi Mudali, T. Nishimura, N. Rajendran, A review on TiO2 nanotubes: influence of anodization parameters, formation mechanism, properties, corrosion behavior, and biomedical applications, J. Bio. Tribo. Corros 1 (2015) 28. https://doi.org/10.1007/s40735-015-0024-x

[18] D, Solís-Casados, L. Escobar-Alarcón, L. Gómez-Oliván, E. Haro-Poniatowski, T. Klimova, Photodegradation of pharmaceutical drugs using Sn-modified TiO2 powders under visible light irradiation. Fuel 198 (2017) 3–10. https://doi.org/10.1016/j.fuel.2017.01.059

[19] C. Fleischer, A. Chatzitakis, and T. Norby, Intrinsic photoelectrocatalytic activity in oriented, photonic TiO2 nanotubes, Mater. Sci. Semicond. Process. 88 (2018) 186–191. https://doi.org/10.1016/j.mssp.2018.08.009

[20] S. K. Saraswat, D. D. Rodene, and R. B. Gupta, Recent advancements in semiconductor materials for photoelectrochemical water splitting for hydrogen production using visible light, Renew. Sustain. Energy Rev. 89 (2018) 228–248. https://doi.org/10.1016/j.rser.2018.03.063

[21] P. Roy, S. Berger, and P. Schmuki, TiO_2 nanotubes: Synthesis and applications, Angew. Chemie - Int. Ed. 50 (2011) 2904–2939.

https://doi.org/10.1002/anie.201001374

[22] A. Chatzitakis et al., Comparison of the photoelectrochemical performance of particulate and nanotube TiO_2 photoanodes, Catal. Today 280 (2017) 14–20. https://doi.org/10.1016/j.cattod.2016.07.017

[23] S. Shen et al., Titanium dioxide nanostructures for photoelectrochemical applications, Prog. Mater. Sci. 98 (2018) 299–385. https://doi.org/10.1016/j.pmatsci.2018.07.006

[24] C. W. Lai and S. Sreekantan, Effect of heat treatment on WO3-loaded TiO2 nanotubes for hydrogen generation via enhanced water splitting, Mater. Sci. Semicond. Process. 16 (2013) 947–954. https://doi.org/10.1016/j.mssp.2013.02.002

[25] G.Mohammadnezhad, M.M. Momeni, F Nasiriani, Enhanced photoelectrochemical performance of tin oxide decorated tungsten oxide doped TiO2 nanotube by electrodeposition for water splitting, J. Electroanal. Chem. 876 (2020) 114505. https://doi.org/10.1016/j.jelechem.2020.114505

[26] S. Palmas, L. Mais, M.Mascia, A. Vacca,Trend in using TiO2 nanotubes as photoelectrodes in PEC processes for wastewater treatment, Curr. Opin. Electrochem. 28 (2021) 100699. https://doi.org/10.1016/j.coelec.2021.100699

[27] J. Wang, X. Nie, W. Wang, Z. Zhao, L.Li Z. Zhang, Single-layer graphene-TiO2 nanotubes array heterojunction as photoanode to enhance the photoelectric of DSSCs, Optik 242 (2021) 167245. https://doi.org/10.1016/j.ijleo.2021.167245

[28] I. Zeydabadi-Nejad, N. Zolfaghari, M.M. Mashhadi, M. Baghani, M. Baniassadi, Anatase TiO2 nanotubes as Li-ion battery anodes: A molecular dynamics study of Li-ion adsorption on anatase nanotubes, Sustain. Energy Technol. Assess. 47 (2021) 101438]. https://doi.org/10.1016/j.seta.2021.101438

[29] D. Regonini, G. Chen, C. Leach, F. J. Clemens, Comparison of photoelectrochemical properties of TiO2 Nanotubes and sol-gel, Electrochim. Acta 213 (2016) 31-36. https://doi.org/10.1016/j.electacta.2016.07.097

[30] N. Tsvetkov, L. Larina, J. K. Kang, O. Shevaleevskiy. Sol-Gel Processed TiO2 Nanotube Photoelectrodes for Dye-Sensitized Solar Cells with Enhanced Photovoltaic Performance, Nanomaterials 10 (2020) 296. https://doi.org/10.3390/nano10020296

[31] S. Kumar, T. Vats, S.N. Sharma, J. Kumar, Investigation of annealing effects on TiO2 nanotubes synthesized by a hydrothermal method for hybrid solar cells, Optik 171 (2018) 492-500. https://doi.org/10.1016/j.ijleo.2018.06.045

[32] F. Guo. J. Liu, W. Zhang, Z. Yu, Y. Liu, W. Liang, Synthesis of Cu,N-doped TiO2 nanotube by a novel magnetron sputtering method and its photoelectric property, Vacuum 165 (2019) 223-231. https://doi.org/10.1016/j.vacuum.2019.04.032

[33] Z. Jedi-Soltanabadi, M. Ghoranneviss, Z. Ghorannevis, H. Akbari, Effect of Ti substrate ion implantation on the physical properties of anodic TiO2 nanotubes, J. Kor, Phys. Soc. 72 (2018) 604–609. https://doi.org/10.3938/jkps.72.604

[34] M. Jarosz, J. Kapusta-KoBodziej, M. Jasku Ba, G.D. Sulka, Effect of different polishing methods on anodic titanium dioxide formation, J. Nanomater. (2015) 29512610. https://doi.org/10.1155/2015/295126

[35] R. Sánchez-Tovar, R.M. Fernández-Domene, D.M. García-García, J. García-Antón, Enhancement of photoelectrochemical activity for water splitting by controlling hydrodynamic conditions on titanium anodization, J. Power Sources 286 (2015) 224-231. https://doi.org/10.1016/j.jpowsour.2015.03.174

[36] R. Sánchez-Tovar, R.M. Fernández-Domene, A. Martínez-Sánchez, E. Blasco-Tamarit, J. García-Antón, Synergistic effect between hydrodynamic conditions

during Ti anodization and acidic treatment on the photoelectric properties of TiO2 nanotubes, J. Catal. 330 (2015) 434 - 441. https://doi.org/10.1016/j.jcat.2015.08.002

[37] J. Borrás Ferrís, R. Sanchez-Tovar, E. Blasco-Tamarit, R. M. Fernández Domene; J. Garcia-Anton, Effect of Reynolds number and lithium cation insertion on titanium anodization, Electrochim. Acta (196) (2016) 24 - 32. https://doi.org/10.1016/j.electacta.2016.02.160

[38] R. Sánchez Tovar, E. Blasco-Tamarit, R.M. Fernández Domene, B. Lucas-Granados, J. Garcia-Anton, Should TiO2 nanostructures doped with Li+ be used as photoanodes for photoelectrochemical water splitting applications?, J. Catal 349 (2017) 41 - 52. https://doi.org/10.1016/j.jcat.2017.03.001

[39] E. Blasco-Tamarit, M.J. Muñoz-Portero, R. Sánchez Tovar, R.M. Fernández Domene, J. Garcia-Anton, Effect of Reynolds number on TiO2 nanosponges doped with Li+ cations, New J. Chem. 42 (2018) 11054 - 11063. https://doi.org/10.1039/C8NJ00800K

[40] J. Borràs-Ferrís, R. Sánchez Tovar, E. Blasco-Tamarit, M.J. Muñoz-Portero, R.M. Fernández-Domene, J. Garcia-Anton, TiO2 Nanostructures for Photoelectrocatalytic Degradation of Acetaminophen, Nanomaterials 9 (2019) 583. https://doi.org/10.3390/nano9040583

[41] E. Blasco-Tamarit, R. Sánchez Tovar, R. M. Fernández Domene, M. Villanueva-Pascual, J. Garcia-Anton, Electrochemical formation of novel TiO2-ZnO hybrid nanostructures for photoelectrochemical water splitting applications, Surf. Coat. Technol.388(2020) 125605-
125615. https://doi.org/10.1016/j.surfcoat.2020.125605

[42] Z. Huaa, Z. Daia, X. Baia, Z. Yeb, H. Gua, X. Huang, A facile one-step

electrochemical strategy of doping iron, nitrogen, and fluorine into titania nanotube arrays with enhanced visible light photoactivity, J. Hazard Mater. 293 (2015) 112–121. https://doi.org/10.1016/j.jhazmat.2015.03.049

[43] M. M. Momeni, Y. Ghayeb, and M. Davarzadeh, Single-step electrochemical anodization for synthesis of hierarchical WO3-TiO2 nanotube arrays on titanium foil as a good photoanode for water splitting with visible light, J. Electroanal. Chem. 739 (2015) 149–155. https://doi.org/10.1016/j.jelechem.2014.12.030

[44] Y. Ma, X. Wang, Y. Jia, X. Chen, H. Han, and C. Li, Titanium Dioxide Based Nanomaterials for Photocatalytic Fuel Generations, Chem. Rev. 114 (2014) 9987–10043. https://doi.org/10.1021/cr500008u

[45] S. Sreekantan, R. Hazan, Z. Lockman, Photoactivity of anatase–rutile TiO2 nanotubes formed by anodization method, Thin Solid Films 518 (2009) 16-21. https://doi.org/10.1016/j.tsf.2009.06.002

[46] M.Nycz1, E. Paradowska, K. Arkusz, D. G. Pijanowska, Influence of geometry and annealing temperature in argon atmosphere of TiO2 nanotubes on their electrochemical properties, Acta Bioeng. Biomech. 22 (2020) 165-177. https://doi.org/10.37190/ABB-01479-2019-03

[47] A. Ghicov, H. Tsuchiya, J.M. Macak, P. Schmuki, Annealing effects on the photoresponse of TiO2 nanotubes, Phys. Stat. Sol. A 203 (2006) 28–30. https://doi.org/10.1002/pssa.200622041

[48] K. Zhu, N.R. Neale, A.F. Halverson, J.Y. Kim, A.J. Frank, Effects of annealing temperature on the charge-collection and light-harvesting properties of TiO2 nanotube-based dye-sensitized solar cells, J. Phys. Chem. C 114 (2010) 13433–13441. https://doi.org/10.1021/jp102137x

[49] M. Wu, K. Hsiao, Y. Chang, S. Chan, Photocatalytic Hydrogen Evolution of

Palladium Nanoparticles Decorated Black TiO2 Calcined in Argon Atmosphere, Appl. Surf. Sci. (2018) 407-414. https://doi.org/10.1016/j.apsusc.2017.08.071

[50] R Plugaru, A Cremades, J Piqueras, The effect of annealing in different atmospheres on the luminescence of polycrystalline TiO2, J. Phys.: Condens. Matter 16 (2004) S261–S268. https://doi.org/10.1088/0953-8984/16/2/031

[51] H. Huang, X.Hou, J. Xiao, L.Zhao, Q. Huang, H. Chen, Y. Li, Effect of annealing atmosphere on the performance of TiO2 nanorod arrays in photoelectrochemical water splitting. Catal. Today 330 (2018) 189-194. https://doi.org/10.1016/j.cattod.2018.04.011

[52] P. Mohanty, D. Kabiraj, R.K. Mandal, P.K. Kulriya, A.S.K. Sinha, Chandana Rath, Evidence of room temperature ferromagnetism in argon/oxygen annealed TiO2 thin films deposited by electron beam evaporation technique, J. Magn. Magn. Mater. 355 (2014) 240–245. https://doi.org/10.1016/j.jmmm.2013.12.025

[53] L. Zeng, W. Song, M. Li, X. Jie, D. Zeng, C. Xie, Comparative study on the visible light driven photocatalytic activity between substitutional nitrogen doped and interstitial nitrogendoped TiO2, Appl. Catal. A- Gen. 488 (2014) 239–247. https://doi.org/10.1016/j.apcata.2014.09.041

[54] X. Yang, C. Cao, K. Hohn, R. Maghirang, K. Klabunde, Synthesis of visible-light-active TiO2-based photocatalysts by carbon and nitrogen doping, J. Catal. 260 (2008) 128-133. https://doi.org/10.1016/j.jcat.2008.09.016

[55] E. Pérez, M. Farfán Torres, G. Morales, V. Murgia, E. Sham, Syntesis of N-TiO2 Effect of the concentration of Nitrogen in the Band Gap, Proc. Mat. Sci. (2015) 649-655. https://doi.org/10.1016/j.mspro.2015.04.121

[56] L. Rizzo, D. Sannino, V. Vaiano, O. Sacco, A. Scarpa, D. Pietrogiacomi, Effect of solar simulated N-doped TiO2photocatalysis on heinactivation and antibiotic

resistance of an E. coli strain in biologicallytreated urban wastewater, Appl. Catal. B-Environ. 144 (2014) 369– 378. https://doi.org/10.1016/j.apcatb.2013.07.033

[57] A. Bjelajac, R. Petrović, M. Popović, Z. Rakočević, G. Socol, I.N. Mihailescu, D. Janaćković, Doping of TiO2 nanotubes with nitrogen by annealing in ammonia for visible light activation: Influence of pre- and post-annealing in air, Thin Solid Films 692 (2019) 137598. https://doi.org/10.1016/j.tsf.2019.137598

[58] S. Horikoshi, Y. Shirasaka, H. Uchida, N. Horikoshi, N. Serpone, Facile preparation of N-doped TiO2 at ambient temperature and pressure under UV light with 4-nitrophenol as the nitrogen source and its photocatalytic activities, Photochem. Photobiol. Sci. 15 (2016) 1061-1070. https://doi.org/10.1039/C6PP00167J

[59] D. Huang, W. Xie, Z. Tu, F. Zhang, S. Quan, L. Liu, N-TiO2/γ-Al2O3 Granules: Preparation, Characterization and Photocatalytic Activity for the Degradation of 2,4-Dichlorophenol, J. Nanosci Nanotechnol. 13 (2013) 260-269. https://doi.org/10.1166/jnn.2013.6846

[60] O.K. Varghese, C.A. Grimes, Appropriate strategies for determining the photoconversion efficiency of water photoelectrolysis cells: a review with examples using titania nanotube array photoanodes, Sol. Energ. Mat. Sol. C. 92 (2008) 374–384. https://doi.org/10.1016/j.solmat.2007.11.006

[61] Z. Zhang, M. Hossain, T. Takahashi, Self-assembled hematite (a-Fe2O3) nanotube arrays for photoelectrocatalytic degradation of azo dye under simulated solar light irradiation, Appl. Catal. B – Environ. 95 (2010) 423–429. https://doi.org/10.1016/j.apcatb.2010.01.022

[62] G. Rahman, O.S. Joo, Photoelectrochemical water splitting at nanostructured a-Fe2O3 electrodes, Int. J. Hydrog. Energy 37 (2012) 13989–13997.

https://doi.org/10.1016/j.jphotochem.2010.07.032

[63] M. Ye, D. Zheng, M. Lv, C. Chen, C. Lin, Z. Lin, Hierarchically structured nanotubes for highly efficient dye-sensitized solar cells, Adv. Mater. 25 (2013) 3039–3044. https://doi.org/10.1002/adma.201205274

[64] R. López, R. Gómez, Band-gap energy estimation from diffuse reflectance measurements on sol-gel and commercial TiO2: a comparative study, J. Sol-Gel. Sci. Technol. 61 (2012) 1–7. https://doi.org/10.1007/s10971-011-2582-9

[65] J. Tauc, A. Menth, D.L. Wood, Optical and magnetic investigations of the localized states in semiconducting glasses, Phys. Rev. Lett. 25 (1970) 749–752. https://doi.org/10.1103/PhysRevLett.25.749

[66] J.H. Park, S. Kim, A.J. Bard, Novel carbon-doped TiO2 nanotube arrays with high aspect ratios for efficient solar water splitting, Nano Lett. 6 (2006) 24–28. https://doi.org/10.1021/nl051807y

[67] L. Wang, C.Y. Lee, P. Schmuki, Influence of annealing temperature on photoelectrochemical water splitting of a-Fe2O3 films prepared by anodic deposition, Electrochim. Acta 91 (2013) 307–313. https://doi.org/10.1016/j.electacta.2012.12.101

[68] X. Zhou, N. Truong Nguyen, S. Özkan, P. Schmuki, Anodic TiO2 nanotube layers: Why does self-organized growth occur- A mini review, Electrochem. Commun. (2014) 157-162. https://doi.org/10.1016/j.elecom.2014.06.021

[69] S. Mohajernia, A. Mazare, E. Gongadze, V. Kralj-Iglič, A. Iglič, P. Schmuki, Self-organized, free-standing TiO2 nanotube membranes: Effect of surface electrokinetic properties on flow-through membranes, Electrochim. Acta 245 (2017) 25-31. https://doi.org/10.1016/j.electacta.2017.05.115

[70] P. Roy, S.P. Albu, P. Schmuki, TiO2 nanotubes in dye-sensitized solar cells:

Higher efficiencies by well-defined tube tops, Electrochem. Commun. 12 (2010) 949-951. https://doi.org/10.1016/j.elecom.2010.04.029

[71] C. B. D. Marien, T. Cottineau, D. Robert, and P. Drogui, TiO2 Nanotube arrays: Influence of tube length on the photocatalytic degradation of Paraquat, Appl. Catal. B Environ. 194 (2016) 1–6. https://doi.org/10.1016/j.apcatb.2016.04.040

[72] A. Mazzarolo, K. Lee, A. Vicenzo, and P. Schmuki, Anodic TiO2 nanotubes: Influence of top morphology on their photocatalytic performance, Electrochem. commun. 22 (2012) 162–165. https://doi.org/10.1016/j.elecom.2012.05.037

[73] Y. Cong, J. Zhang, F. Chen, M. Anpo, Synthesis and Caracterization of Nitrogen-Doped TiO2 Nanophotocatalyst with High Visible Ligth Activity, J. Phys. Chem. C (2007) 6976-6982. https://doi.org/10.1021/jp0685030

[74] L. Qian, Z.L. Du, S.Y. Yang, Z.S. Jin, Raman study of titania nanotube by soft chemical process, J. Mol. Struct. 749 (2005) 103–107. https://doi.org/10.1016/j.molstruc.2005.04.002

[75]] S. Mozia, E. Borowiak-Palen, J. Przepiórski, B. Grzmil, T. Tsumura, M. Toyoda, J. Grzechulska-Damszel, A.W. Morawski, Physico-chemical properties and possible photocatalytic applications of titanate nanotubes synthesized via hydrothermal method, J. Phys. Chem. Solids 71 (2010) 263–272. https://doi.org/10.1016/j.jpcs.2009.12.074

[76] H.W. Cho, K.L Liao, J.S. Yang, J.J Wu, Revelation of rutile phase by Raman scattering for enhanced photoelectrochemical performance of hydrothermally-grown anatase TiO2 film, Appl. Surf. Sci. 440 (2018) 125-132. https://doi.org/10.1016/j.apsusc.2018.01.139

[77] Z. Wei, C. Hsu, H. Almakrami, G. Lina, J. Hu, X. Jin, E. Agar, F. Liu, Ultra-high-aspect-ratio vertically aligned 2D MoS2-1D TiO2 nanobelt heterostructured

forests for enhanced photoelectrochemical performance, Electrochim. Acta 316 (2019) 173-180. https://doi.org/10.1016/j.electacta.2019.04.090

[78] L. Lin, Y. Yang, L. Men, X. Wang, D. He, Y. Chai, B. Zhao, S. Ghoshroy, Q. Tang, A highly efficient TiO2@ZnO n–p–n heterojunction nanorod photocatalyst, Nanoscale 5 (2013) 588-593. https://doi.org/10.1039/C2NR33109H

[79] A. Kushwaha, M. Aslam, ZnS shielded ZnO nanowire photoanodes for efficient water splitting, Electrochim. Acta 130 (2014) 222–231. https://doi.org/10.1016/j.electacta.2014.03.008

[80] A. Kushwaha, H. Tyagi, M. Aslam, Role of defect states in magnetic and electrical properties of ZnO nanowires, AIP Adv. 3 (2013) 042110–042115. https://doi.org/10.1063/1.4801937

[81] J. Liqiang, S. Xiaojun, X. Baifu, W. Baiqi, C. Weimin, F. Honggang, The preparation and characterization of La doped TiO2 nanoparticles and their photocatalytic activity, J. Solid State Chem. 177 (2004) 3375-3382. https://doi.org/10.1016/j.jssc.2004.05.064

[82] X. Cheng, X. Yu a, Z. Xing, J. Wan, Enhanced Photocatalytic Activity of Nitrogen Doped TiO2 Anatase Nano-Particle under Simulated Sunligth Irradiation. Energy Proc. (2011) 598-605. https://doi.org/10.1016/j.egypro.2012.01.096

[83] J.H. Yang, K.H. Kim, C.W. Bark, H.W. Choi, The effect of dye-sensitized solar cell based on the composite layer by anodic TiO2 nanotubes, Nanoscale Res Lett. 9 (2014) 671. https://doi.org/10.1186/1556-276X-9-671

[84] P.M. Perillo, D.F. Rodríguez, Photocatalysis of Methyl Orange using free standing TiO2 nanotubes under solar light, Environ. Nanotechnol. Monit. Manag.16 (2021) 100479 . https://doi.org/10.1016/j.enmm.2021.100479

[85] P. Bamola, C. Dwivedi, A. Gautam, M. Sharma, H. Sharma, Strain-induced

bimetallic nanoparticles-TiO2 nanohybrids for harvesting light energy, Appl. Surf. Sci. 511 (2020), p. 145416. https://doi.org/10.1016/j.apsusc.2020.145416

[86] S.A. Abdullah, M.Z. Sahdan, N. Nayan, Z. Embong, C.H. Cik Rohaida, F. Adriyanto, Neutron beam interaction with rutile TiO2 single crystal (1 1 1): Raman and XPS study on Ti3+-oxygen vacancy formation, Mater. Lett. 263 (2020) 127143. https://doi.org/10.1016/j.matlet.2019.127143

[87] S.A. Abdullah, M.Z. Sahdan, N. Nafarizal, H. Saim, Z. Embong, C.H. Cik Rohaida, F. Adriyanto, Influence of substrate annealing on inducing Ti3+ and oxygen vacancy in TiO2 thin films deposited via RF magnetron sputtering, Appl. Surf. Sci. 462 (2018) 575-582. https://doi.org/10.1016/j.apsusc.2018.08.137

[88] A. Ghobadi, T.G. Ulusoy, R. Garifullin, M.O. Guler, A.K. Okyay, Heterojunction Design of Single Layer Hole Tunneling ZnO Passivation Wrapping around TiO2 Nanowires for Superior Photocatalytic Performance, Scie. Rep. 6 (2016) 30587. https://doi.org/10.1038/srep30587

[89] A.P. Shpak, A.M. Korduban, M.M. Medvedskij, V.O. Kandyba, XPS studies of active elemets surface of gas sensors based on WO3- nanoparticles, J. Electron Spectros. Relat. Phenomena 156-158 (2007) 172–175, https://doi.org/10.1016/j.elspec.2006.12.059

[90] L. Wang, X. Xu, S. Wu, F. Cao, Nonstoichiometric tungsten oxide residing in a 3D nitrogen doped carbon matrix, a composite photocatalyst for oxygen vacancy induced VOC degradation and H2 production. Catal. Sci. Technol. 8 (2018) 1366–1374, https://doi.org/10.1039/c7cy02572f.

[91] J.C. Hsu, Y.H. Lin, P.W. Wang, X-ray Photoelectron Spectroscopy Analysis of Nitrogen-Doped TiO2 Films Prepared by Reactive-Ion-Beam Sputtering with Various NH3/O2 Gas Mixture Ratios, Coatings 10 (2020) 47.

https://doi.org/10.3390/coatings10010047

[92] A.T. Zajac, M. Radecka, K. Zakrzewska, A. Brudnik, E. Kusior, S. Bourgeois, M.C. Marco de Lucas, L. Imhoff, Structural and electrical properties of magnetron sputtered Ti(ON) thin films: The case of TiN doped in situ with oxygen. J. Power Sources 194 (2009) 93–103. https://doi.org/10.1016/j.jpowsour.2008.12.112

[93] A.B. Panda, P. Laha, K. Harish, B. Sarkar, S.V. Chaure, W.A. Sayyad, V.S. Jadhav, G.R. Kulkarni, D. Sasmal, P.K. Barhai, A.K. Das, S.K. Mahapatra, I. Barnejee, Study of bactericidal efficiency of magnetron sputtered TiO2 films deposited at varying oxygen partial pressure. Surf. Coat. Tech. 205 (2010) 1611–1617. https://doi.org/10.1016/j.surfcoat.2010.07.101

[94] S.h. Cheung, P. Nachimuthu, A.G. Joly, M.H. Engelhard, M.K. Bowman, S.A. Chambers, N incorporation and electronic structure in N-doped TiO2 (110) rutile, Surf. Sci. 601 (2007) 1754-1762. https://doi.org/10.1016/j.susc.2007.01.051

[95] F. Peng, L. Cai, L. Huang, H. Yu, H. Wang, Preparation of nitrogen-doped titanium dioxide with visible-light photocatalytic activity using a facile hydrothermal method, J. Phys. Chem. Solids 69 (2008) 1657–1664. https://doi.org/10.1016/j.jpcs.2007.12.003

[96] L.K. Tsui, T. Homma, G. Zangari, Photocurrent Conversion in Anodized TiO2 Nanotube Arrays: Effect of the Water Content in Anodizing Solutions, J. Phys. Chem C 117 (2013) 6979-6989. https://doi.org/10.1021/jp400318n

[97] L. Aïnouche, L. Hamadou, A. Kadri, N. Benbrahim, D. Bradai, Interfacial Barrier Layer Properties of Three Generations of TiO2 Nanotube Arrays, Electrochim. Acta 133 (2014) 597-609. https://doi.org/10.1016/j.electacta.2014.04.086

[98] L.Haryński, J. Karczewski, J. Ryl, K. Grochowska, K. Siuzdak, Rapid development of the photoresponse and oxygen evolution of TiO2 nanotubes sputtered with Cr

thin films realized via laser annealing, J. Alloys Compd. 877 (2021) 160316. https://doi.org/10.1016/j.jallcom.2021.160316

[99] M. Motola, R. Zazpe, L. Hromadko, J. Prikryl, J. M. MacakAnodic, TiO2 nanotube walls reconstructed: Inner wall replaced by ALD TiO2 coating, Appl. Surf. Sci.549 (2021) 149306. https://doi.org/10.1016/j.apsusc.2021.149306

[100] D.S. Kong, W.H. Lu, Y.Y. Feng, Z.Y. Yu, J.X. Wu1, W.J. Fan, H.Y. Liu, Studying on the Point-Defect-Conductive Property of the Semiconducting Anodic Oxide Films on Titanium, J. Electrochem. Soc. 156 (2009) C39-C44. https://doi.org/10.1149/1.3021008

[101] S. Palmas, M. Polcaro, J. Rodriguez, A. Da Pozzo, M. Mascia, A. Vacca, TiO2 photoanodes for electrically enhanced water splitting, Int. J. Hydrogen Energy 35 (2010) 6561-6570. https://doi.org/10.1016/j.ijhydene.2010.04.039

[102] D. Sazou, K. Saltidou, M. Pagitsas, Understanding the effect of bromides on the stability of titanium oxide films based on a point defect model, Electrochim. Acta 76 (2012) 48-61. https://doi.org/10.1016/j.electacta.2012.04.158

[103] D. Tafalla, P. Salvador, and R. M. Benito, Kinetic Approach to the Photocurrent Transients in Water Photoelectrolysis at n-TiO2 Electrodes, J. Electrochem. Soc. 137 (1990) 1810–1815. https://doi.org/10.1149/1.2086809

[104] C. W. Lai, S. Sreekantan, Preparation of hybrid WO3-TiO2 nanotube photoelectrodes using anodization and wet impregnation: Improved water-splitting hydrogen generation performance, Int. J. Hydrog. Energy 38 (2013) 2156–2166. https://doi.org/10.1016/j.ijhydene.2012.12.025

[105] R.S. Vemuri, M. Noor-A-Alam, S.K. Gullapalli, M.H. Engelhard, C.V. Ramana, Nitrogen-incorporation induced changes in the microstructure of nanocrystalline WO3 thin films, Thin Solid Films 520 (2011) 1446–1450.

https://doi.org/10.1016/j.tsf.2011.08.080

[106] S. Valencia, J.M. Marín, G. Restrepo, Study of the bandgap of synthesized titanium dioxide nanoparticules using the sol-gel method and a hydrothermal treatment, Open Mater. Sci. 4 (2009) 9–14. https://doi.org/10.2174/1874088X01004010009

[107] F.M. Hossain, L. Sheppard, J. Nowotny, G.E. Murch, Optical properties of anatase and rutile titanium dioxide: Ab initio calculations for pure and aniondoped material, J. Phys. Chem. Solids 69 (2008) 1820–1828. https://doi.org/10.1016/j.jpcs.2008.01.017

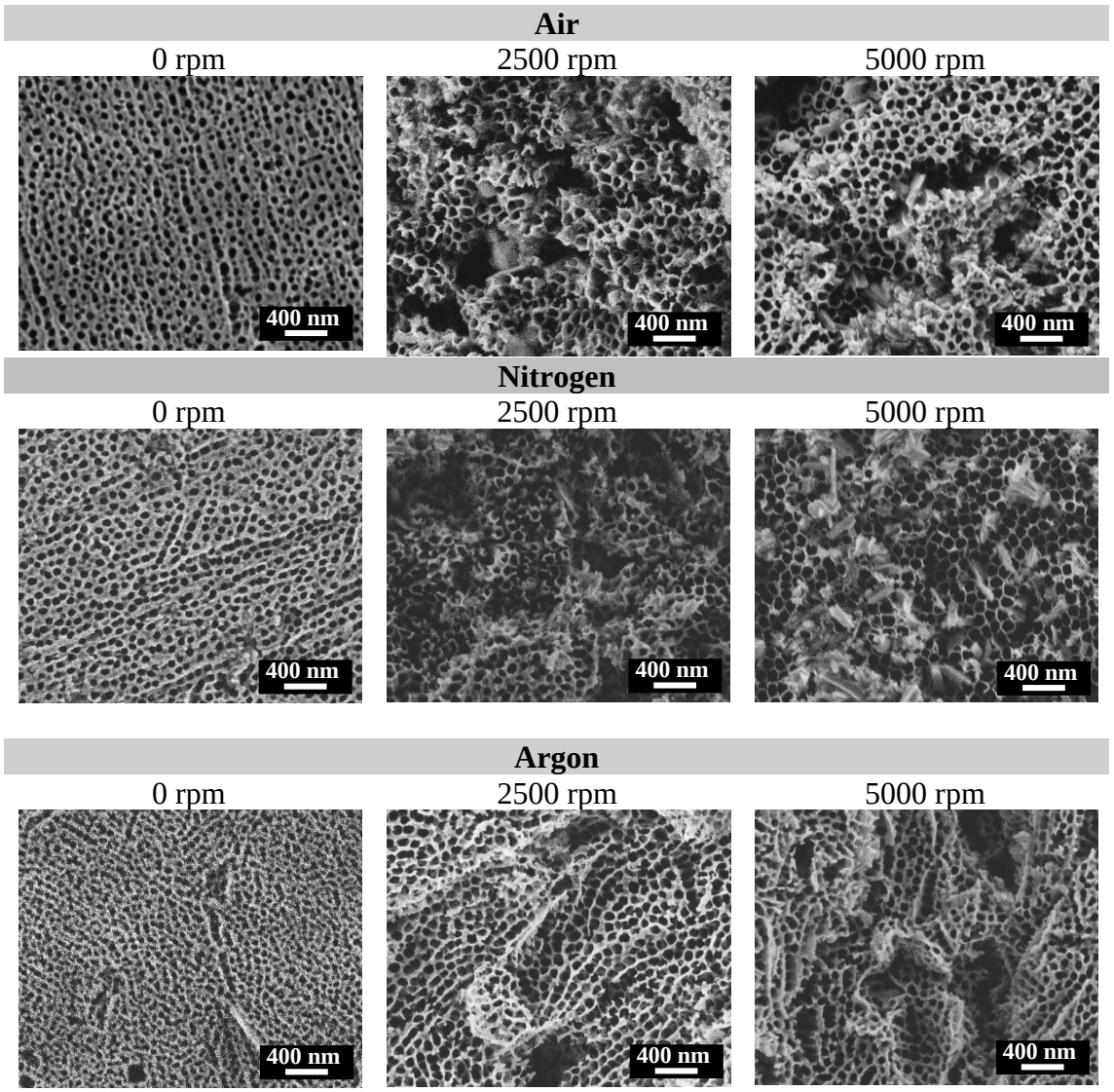

Figure 1. FE-SEM images of the nanostructures obtained under different hydrodynamic conditions during anodization and annealing atmospheres (air, nitrogen and argon).

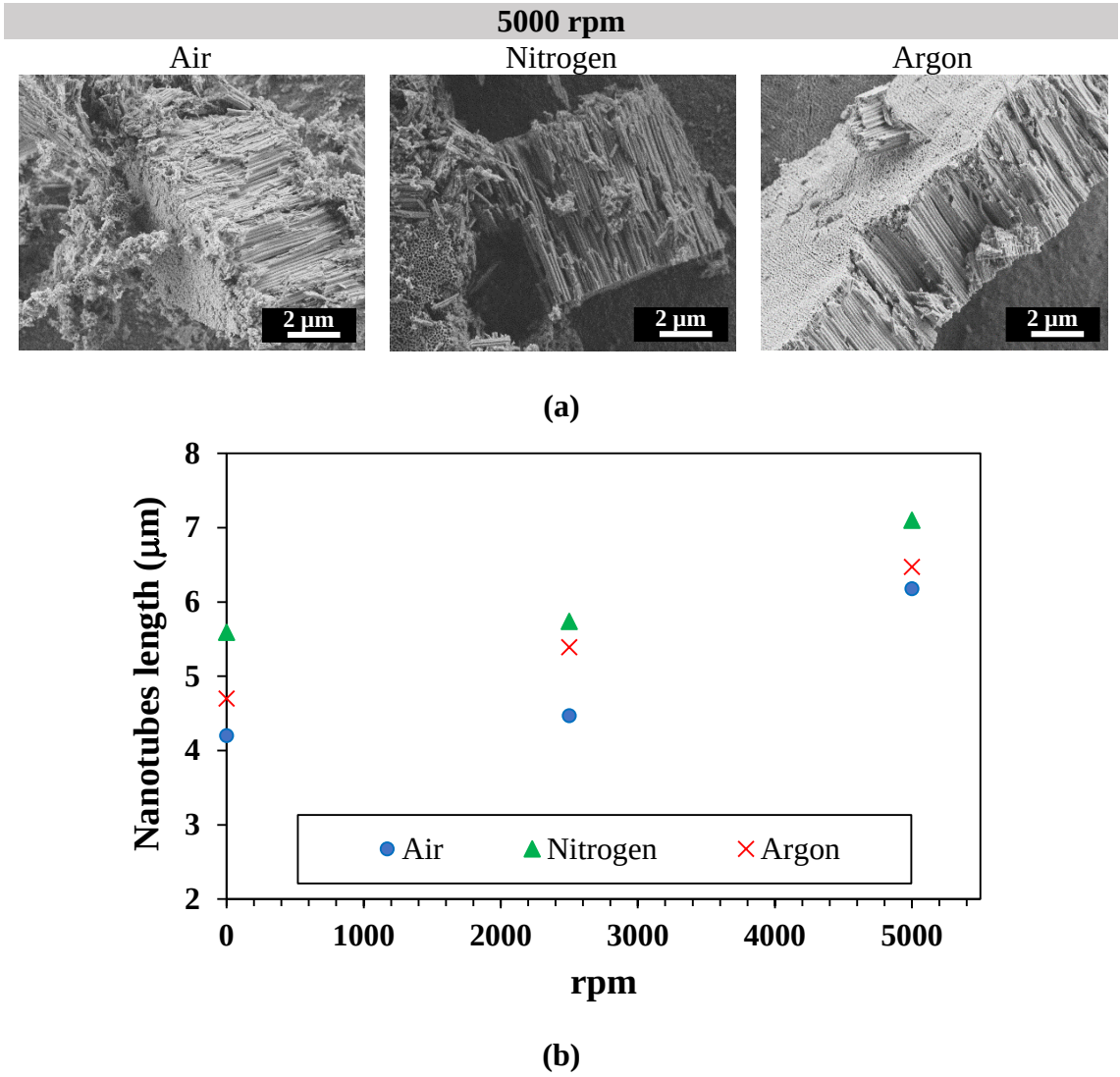

Figure 2. (a) FE-SEM images of the cross section of the TiO_2 nanotubes anodized at 5000 rpm under the different heat treatments (air, nitrogen and argon). (b) Nanotubes length as a function of the rotation speed (rpm) for the nanostructures obtained under the different heat treatments (air, nitrogen and argon).

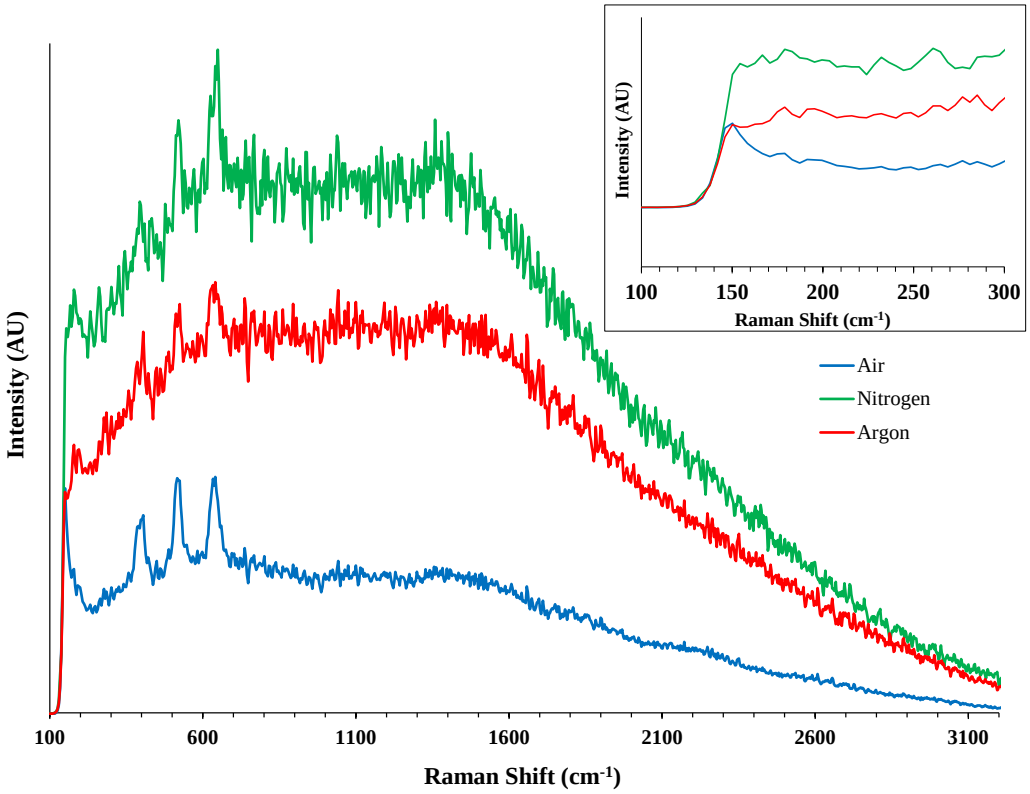

Figure 3. Raman confocal laser spectra of TiO_2 nanostructures anodized at 5000 rpm and annealed in different atmospheres (air, nitrogen and argon).

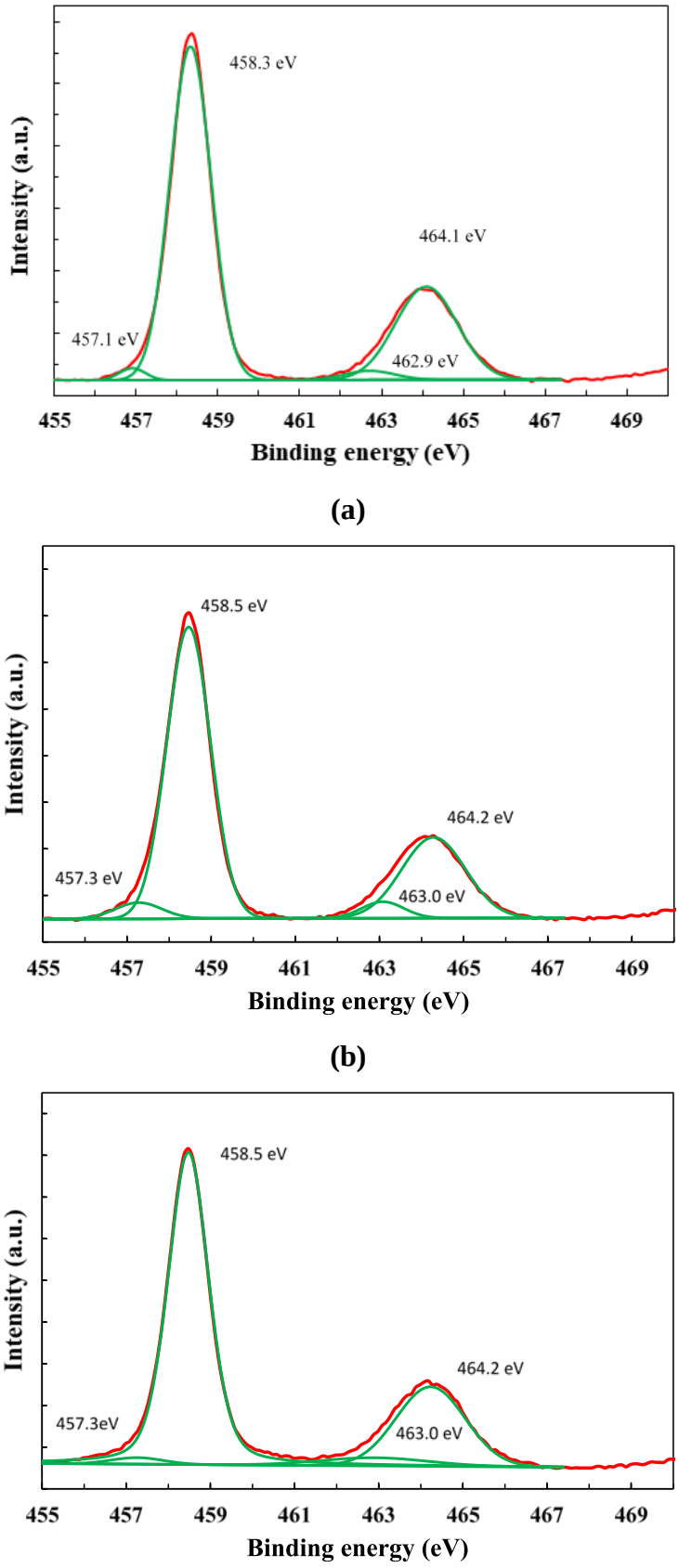

Figure 4. XPS spectra of Ti 2p for the TiO_2 nanostructures anodized at 5000 rpm and annealed in air atmosphere (a), nitrogen atmosphere (b) and argon atmosphere (c).

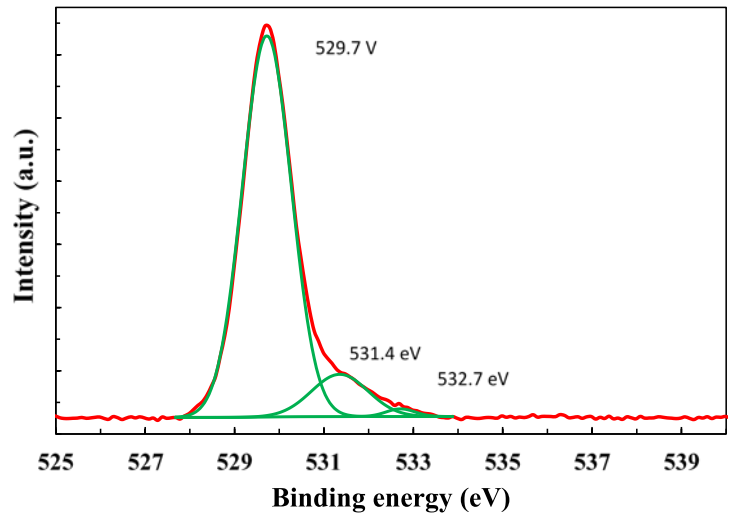

(a)

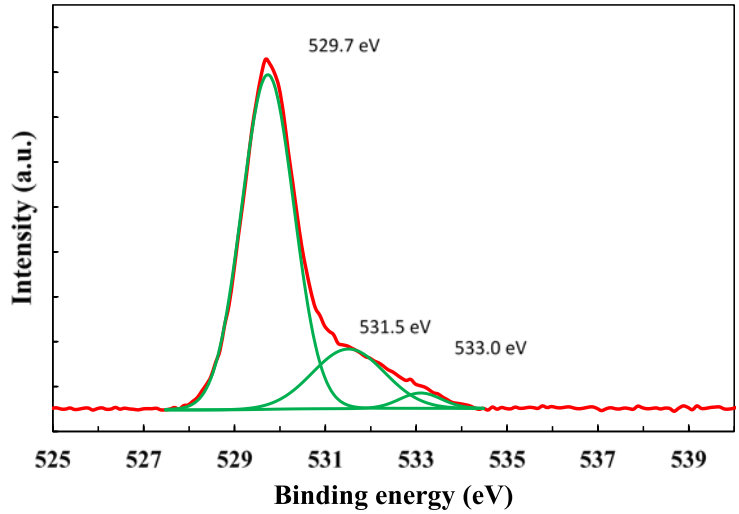

(b)

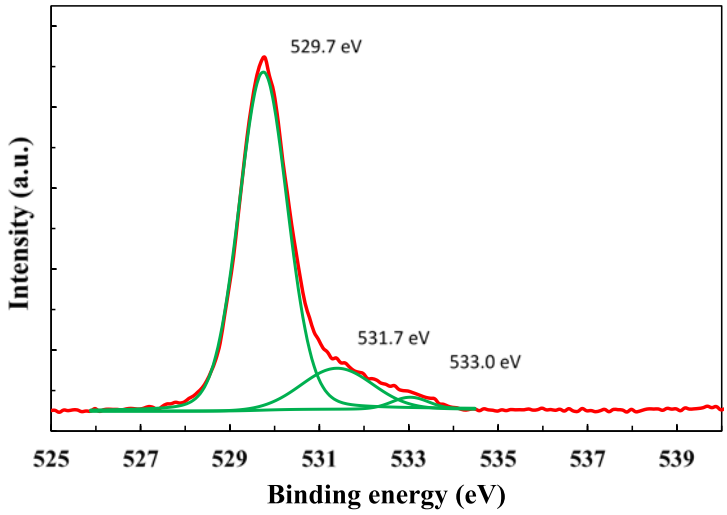

(c)

Figure 5. XPS spectra of O 1s for the TiO_2 nanostructures anodized at 5000 rpm and annealed in air atmosphere (a), nitrogen atmosphere (b) and argon atmosphere (c).

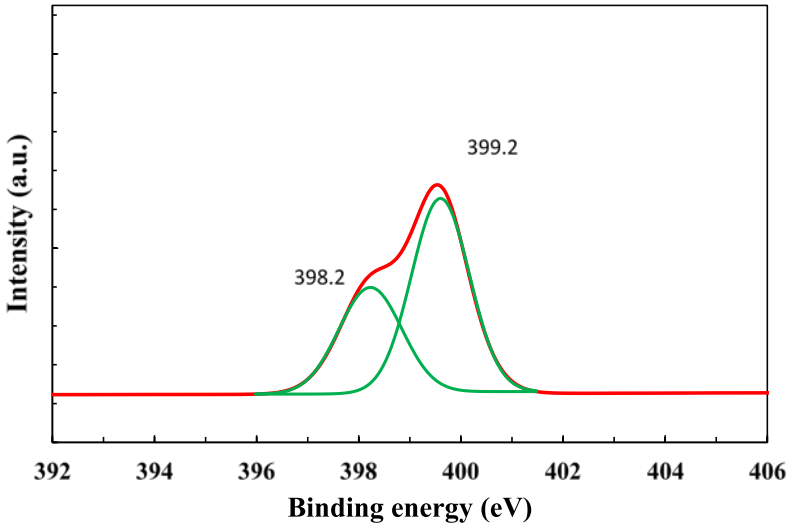

(a)

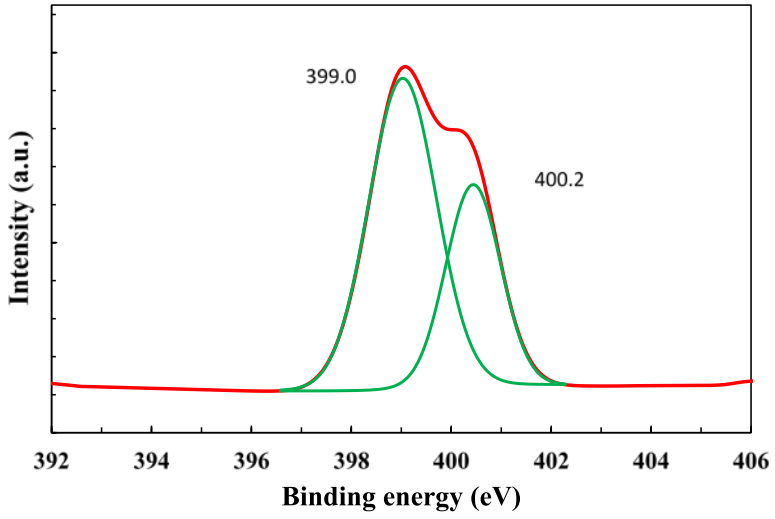

(b)

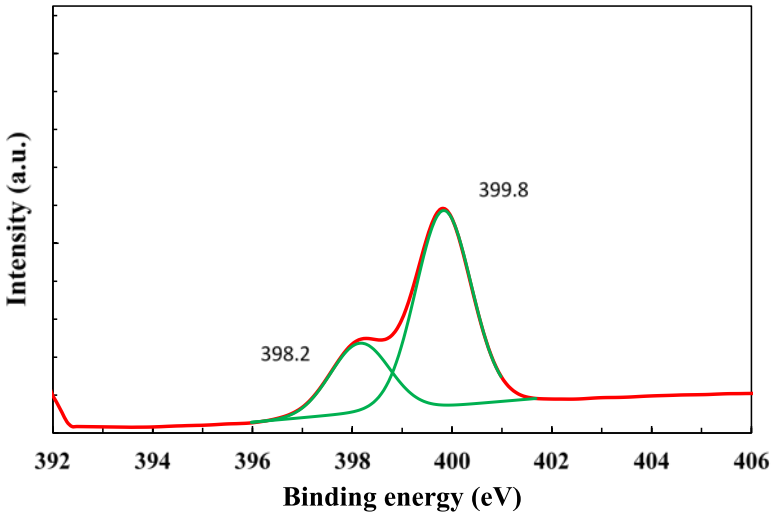

(c)

Figure 6. XPS spectra of N 1s for the TiO_2 nanostructures anodized at 5000 rpm and annealed in air atmosphere (a), nitrogen atmosphere (b) and argon atmosphere (c).

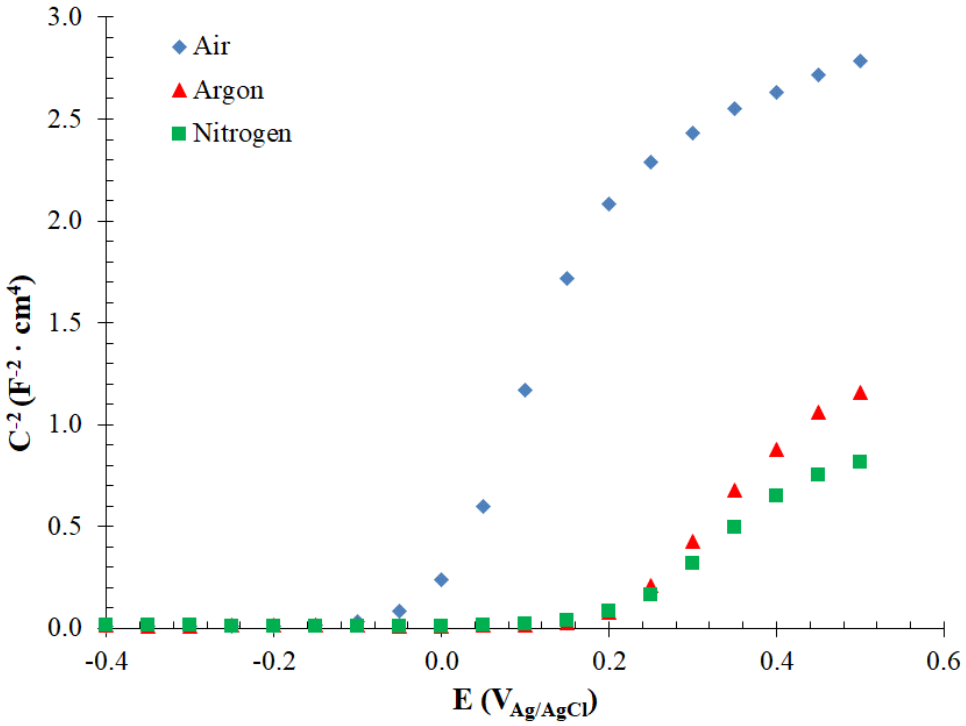

Figure 7. Mott-Schottky plots for the nanostructures anodized at a rotation speed of 5000 rpm and annealed in air, argon and nitrogen.

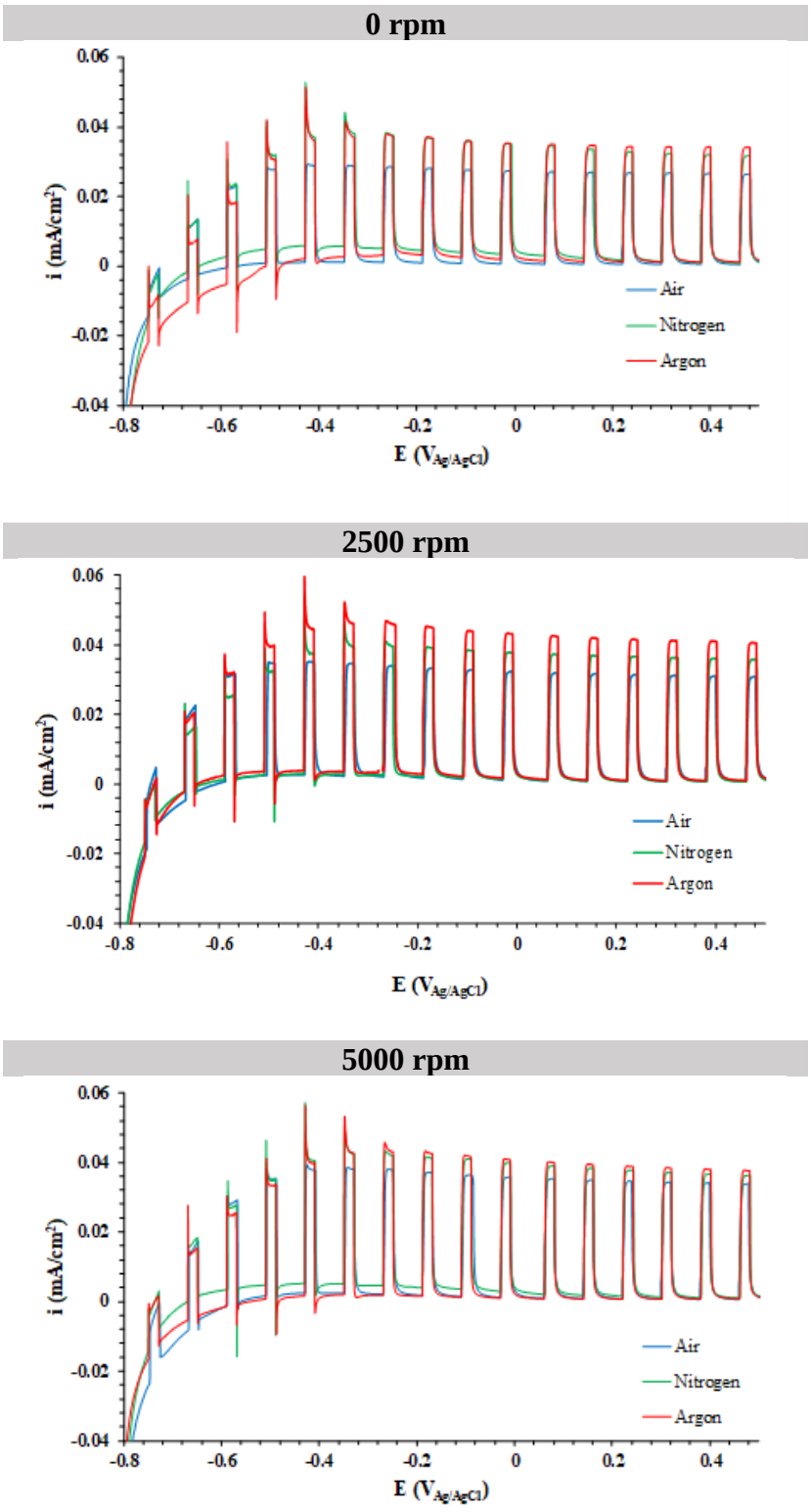

Figure 8. Water splitting measurements for the nanostructures anodized at different rotation speeds (0, 2500 and 5000 rpm) and annealed under different atmospheres (air, nitrogen and argon).

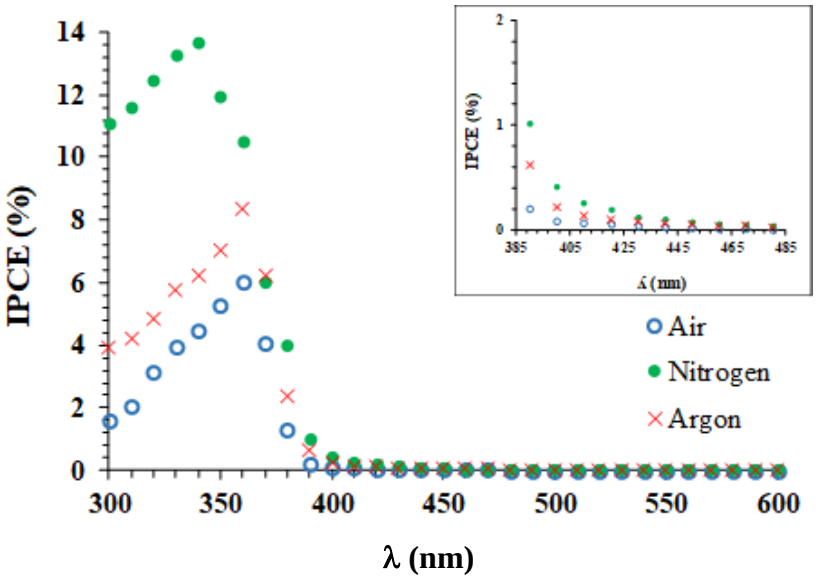

(a)

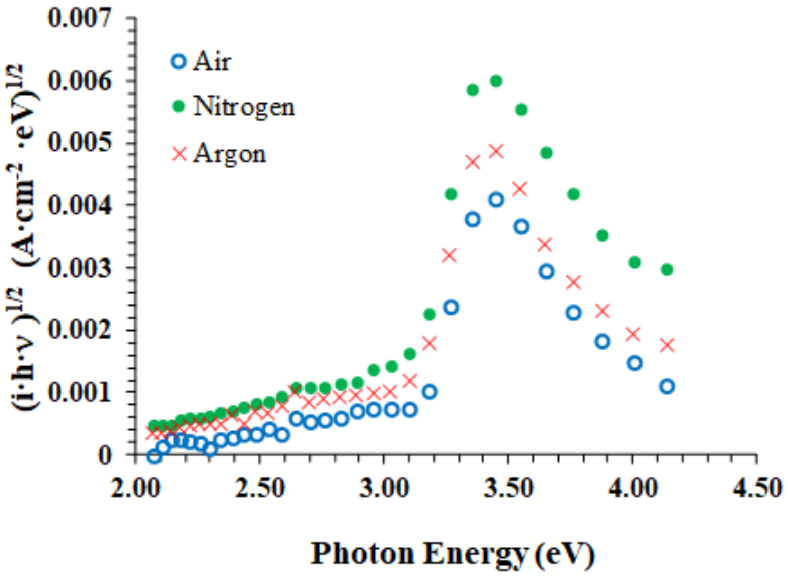

(b)

Figure 9. (a) Incident photon-to-electron conversion efficiency and (b) band gap measurements obtained from IPCE tests of the nanostructures anodized at 5000 rpm and annealed under different atmospheres (Air, Nitrogen and Argon).

Table 1. Ti^{4+} and Ti^{3+} at.% obtained from the XPS areas of the nanostructures anodized at 5000 rpm and annealed in air, nitrogen and argon atmospheres.[a]

	Ti^{3+} (area %)	**Ti^{4+} (area %)**
Air	4.85	95.15
Nitrogen	8.70	91.30
Argon	7.95	92.05

[a] Both $2p_{3/2}$ (Ti^{3+} at 457.1 - 457.3 eV or Ti^{4+} at 458.3 – 458.5 eV) and $2p_{1/2}$ (Ti^{3+} at 462.9 - 463 eV or Ti^{4+} at 464.1 – 464.2 eV) have been considered for the calculation

Table 2. Relative amount of the different surface oxygen species (area %) obtained from the XPS areas of the nanostructures anodized at 5000 rpm and annealed in air, nitrogen and argon atmospheres.

	O 1s 529.7 eV (area %)	**O 1s 531.4 – 531.7 eV (area %)**	**O 1s 532.7 – 533 eV (area %)**
Air	88.70	10.26	1.04
Nitrogen	78.05	19.09	2.86
Argon	83.90	14.03	2.07

Table 3. N 1s peak areas obtained from XPS measurements of the nanostructures anodized at 5000 rpm and annealed in air, nitrogen and argon atmospheres.

	N 1s (398.2 -399.0 eV)	**N 1s (399.2- 400.2 eV)**	**Low BE/High BE ratio**
Air	168	286	0.59
Nitrogen	557	289	1.93
Argon	108	284	0.38

Table 4. Band gap values (in eV) of the nanostructures obtained under different hydrodynamic conditions during anodization and annealed in air, nitrogen and argon atmospheres.

	Air	**Nitrogen**	**Argon**
0 rpm	3.14	2.97	3.08
2500 rpm	3.16	2.99	3.04
5000 rpm	3.10	2.96	3.02

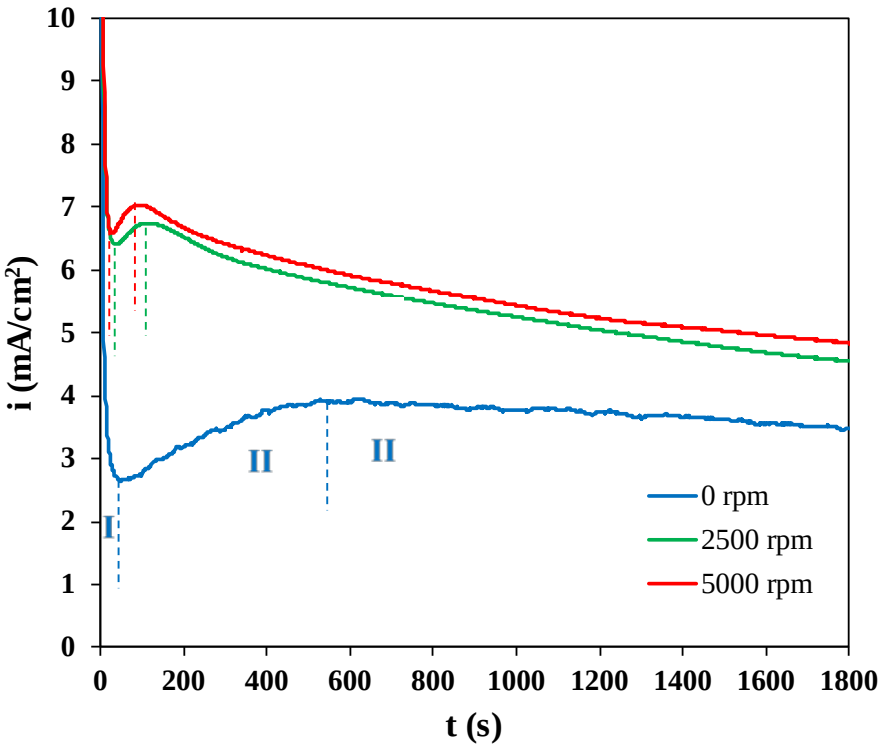

Figure S1. Current densities vs time obtained during anodization of titanium under stagnant (0 rpm) and hydrodynamic conditions (2500 rpm and 5000 rpm).

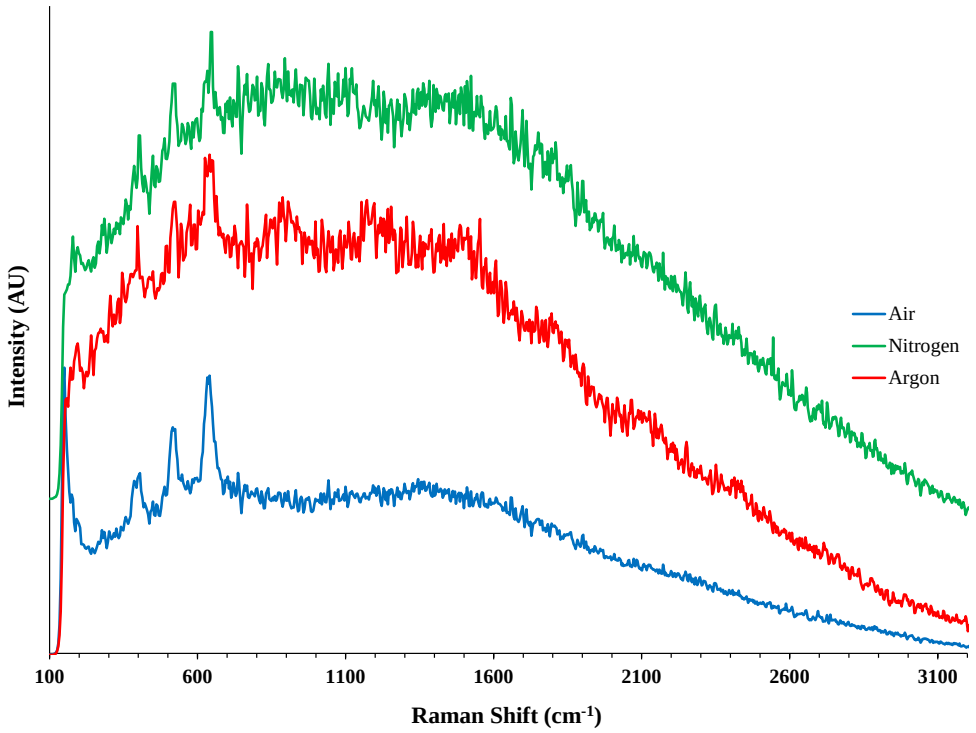

(a)

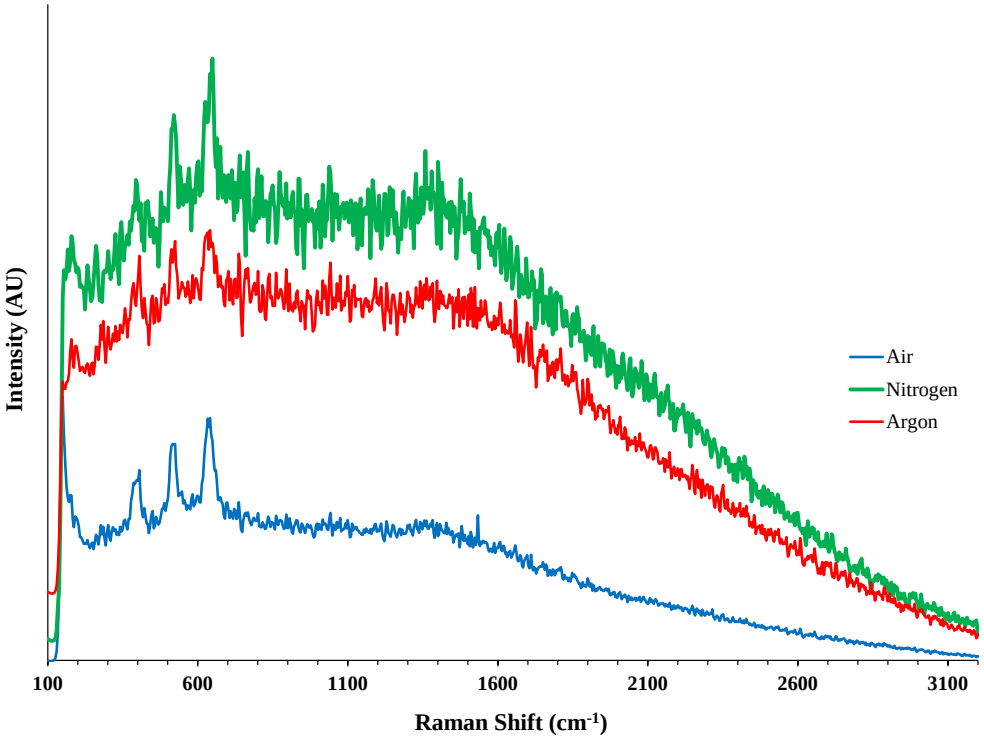

(b)

Figure S2. Raman confocal laser spectra of TiO_2 nanostructures anodized at 0 rpm (a) and 2500 rpm (b) and annealed in different atmospheres (air, nitrogen and argon).

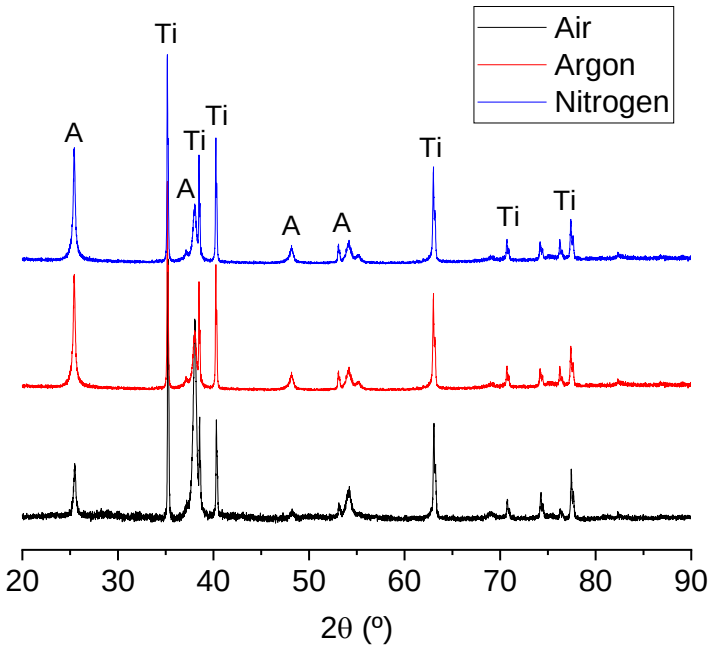

Figure S3. XRD patterns for TiO_2 nanotubes anodized at 5000 rpm after annealing treatment in air, argon and nitrogen atmospheres. Crystalline phases: A: anatase TiO_2, Ti: metallic titanium.

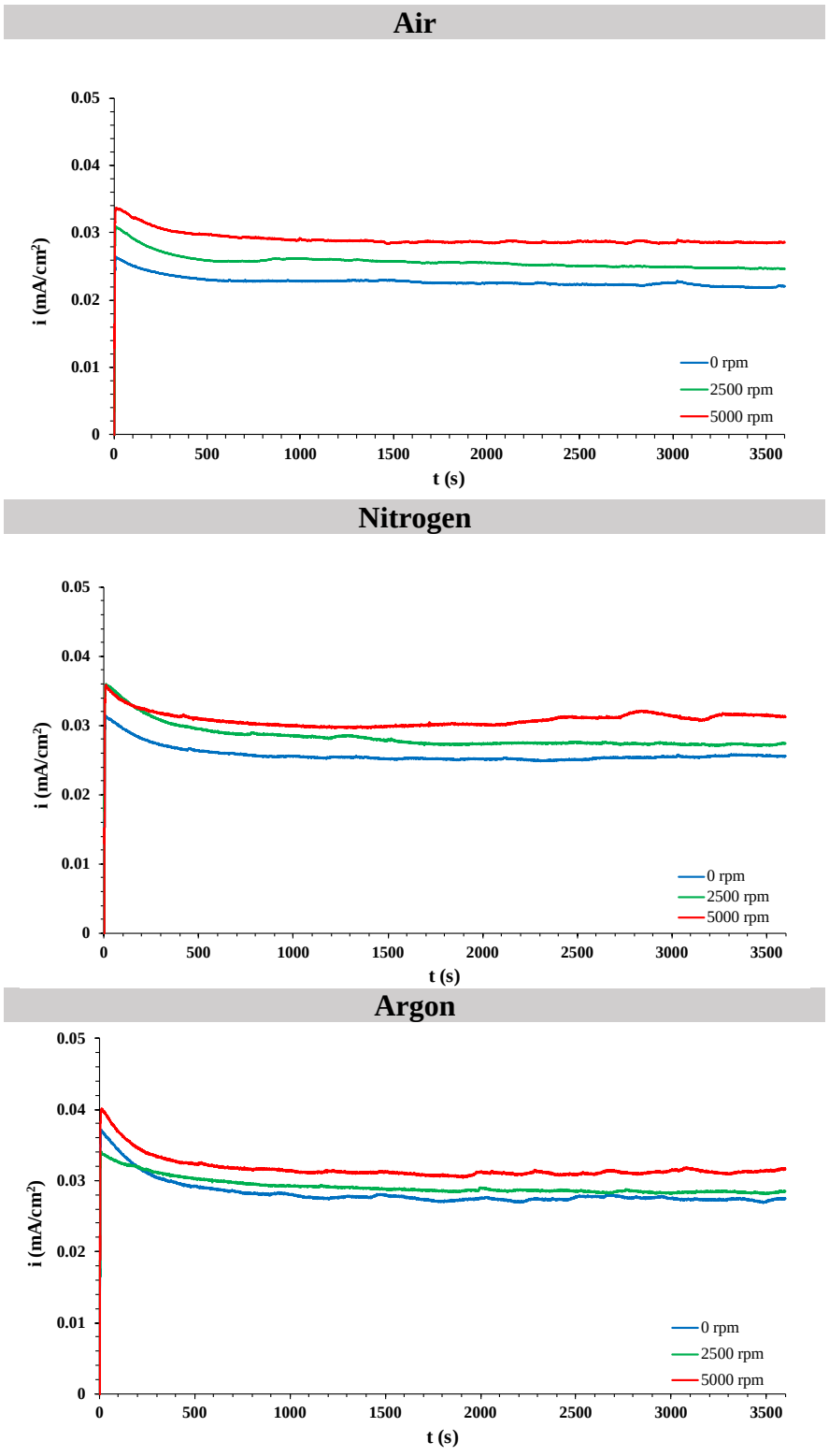

Figure S4. Photostability measurements obtained under a constant potential of 0.5 $V_{Ag/AgCl}$ for the nanostructures anodized at different rotation speeds (0, 2500 and 5000 rpm) and annealed under different atmospheres (Air, Nitrogen and Argon).

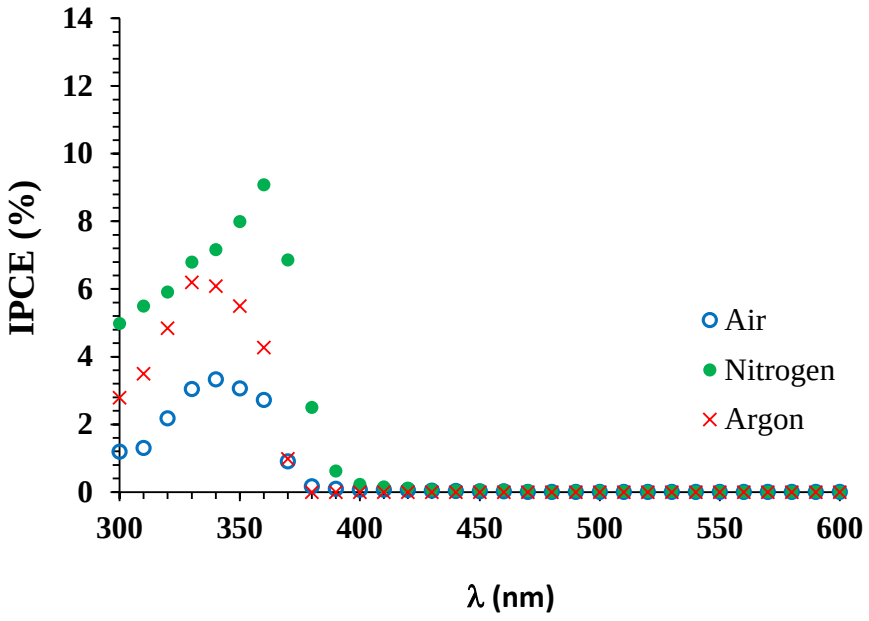

(a)

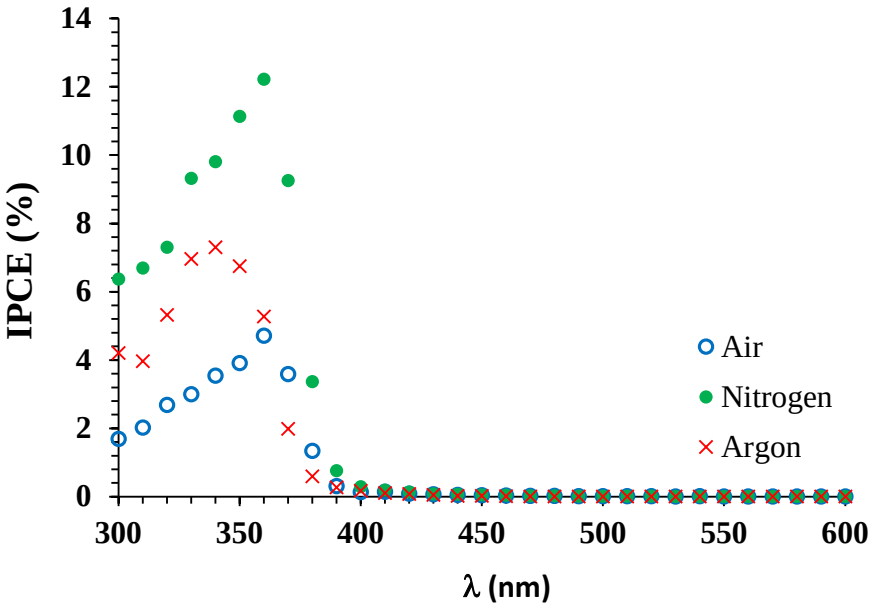

(b)

Figure S5. Incident photon-to-electron conversion efficiency measurements of samples anodized at 0 rpm (a) and 2500 rpm (b) and annealed under different atmospheres (Air, Nitrogen and Argon).